Using two-way nesting technique AGRIF with MARS3D V11.2 to improve hydrodynamics and estimate environmental indicators

Sébastien Petton[1], Valérie Garnier[2], Matthieu Caillaud[3], Laurent Debreu[4], Franck Dumas[5]

[1]Ifremer, Univ Brest, CNRS, IRD, LEMAR, 11 Presqu'île du Vivier, F-29840 Argenton, France
[2]Ifremer, Univ Brest, CNRS, IRD, LOPS, 1625 Route de Sainte-Anne, F-29280 Plouzané, France
[3]Ifremer, DYNECO, 1625 Route de Sainte-Anne, F-29280 Plouzané, France
[4]INRIA, Univ Grenoble Alpes, CNRS, LJK, F-38000 Grenoble, France
[5]SHOM / STM / REC, 13 Rue de Châtellier CS 92803, 29228 Brest CEDEX 2, France

Correspondence to: Sébastien Petton (sebastien.petton@ifremer.fr)

Abstract. In the ocean, meso / submesoscale structures and coastal processes are associated with fine scales. The simulation of such features thus requires the hydrodynamic equations to be solved at high-resolution (from a few hundred meters down to a few tens of meters). Therefore, local mesh refinement is a primary issue for regional and coastal modelling. As over structured grids, AGRIF (Adaptive Grid Refinement In Fortran) library is committed to tackle this challenge. It has been implemented in MARS3D, which is a numerical model developed by Ifremer (the French Research Institute for Exploitation of the Sea) for coastal environmental researches and studies. The present paper describes how the dedicated implementation preserves some essential properties (mass and momentum conservations) along with the induced constraints (need of bathymetric coherence, increase in computation cost). The use and the performance of this new tool are detailed over two configurations that illustrate the wide range of scales and resolutions typically targeted by coastal applications. The first one is based on multiple high-resolution (500m) grids that pave the coastal ocean over thousands of kilometres, allowing a continuum between the regional and coastal scales. The second application is more local and has a finer resolution (50m). It targets a recurrent question for semi-enclosed bays: the renewal time indicator. Throughout these configurations, the paper intends to compare the two-way nesting method with the traditional one-way approach and highlights how the MARS3D-AGRIF tool proves to be an efficient way to significantly improve the physical hydrodynamics and unravel ecological challenges.

1. Introduction

In the ocean, many observations have clearly shown that turbulence is ubiquitous and that flows are turbulent at all scales (Capet, 2015). It is also admitted that capturing the whole range of oceanic scales is far beyond the capabilities of any numerical model for a long time to come. Even Large Eddy Simulation (LES) approach dedicated to solve the direct forward turbulent energy cascade is far from being reachable except for strict localized places. Therefore, it is necessary not only to develop relevant and efficient parametrizations at the subgrid scale, but also to propose refinement capabilities in ocean models in order

to focus the computational grid at key locations. A key region can vary considerably based on geographic or dynamical considerations. As the circulation is obviously tightly controlled by the coastline and more generally by the bathymetry, increasing the resolution of the grid may be essential to properly catch the coastal morphology (e.g., estuaries, cape, peninsulas,

35 small bays and lagoons...). Alternatively, a key region may be an area where essential processes take place that shape the circulation or a fate of a coastal discharge, even far offshore. The Strait of Gibraltar, where internal jump and consequently an internal solitary wave train are generated, is a perfect illustration, as these features propagate for hundreds of kilometers (Naranjo et al., 2014) until they break and reinforce mixing. Thus, the generating area must be addressed with both sufficient resolution and even locally adapted physics (here non-hydrostatic) to reproduce such structures. Then they must be accurately

40 propagated, possibly outside the refined area.

Multiple strategies can be investigated (and are available with some degree of efficiency and accuracy) to tackle the spatial refinement in limited areas. A first one relies on unstructured grids together with finite volume or finite element discretizations: numerous models such as Delft-3D (Roelvink and van Banning, 1995), SLIM (Delandmeter et al., 2018), SYMPHONIE (Marsaleix et al., 2006), TELEMAC-3D (Janin et al., 1993) or T-UGOm (Piton et al., 2020) have shown for years their

45 capability to cope with complex geometrical features such as river deltas or continental slope. A second one is based on curvilinear either orthogonal (Diaz et al., 2020; Rétif et al., 2014… among many others) or non-orthogonal (Grasso et al., 2018) grid. The design of such structured curvilinear grid might be a great deal of work with a lack of flexibility.

In addition to the need to create efficient tools to manage the grid building, this kind of approach has also raised the classical issues related to continuously adaptive subgrid parametrization: how to manage both temporal and spatial refinements so that

50 computational cost required by the finest grid cells does not spill over to the entire grid? Recently Li (2021) proposed a 2D shallow water mode discretized on a regional spherical multiple-cell which circumvents this constraint. An alternative method applies to structured grids and provides a refinement capability (adaptive or not) to integrate recursively a hierarchy of grids at different resolutions. This kind of approach was proposed in the early eighties (Berger and Oliger, 1984) and has already been implemented in either academic works (Penven et al., 2006; Debreu et al., 2012) or for large-scale realistic applications

55 (Biastoch et al., 2009; Marchesiello et al., 2011) to improve the resolution and hence the realism of the local dynamics.

Such an approach, the Adaptive Grid Refinement In Fortran (AGRIF) (Debreu et al., 2008), is based on domain decomposition and needs partial overlapping of same level grids. Despite the overlapping constraint, it is expected to facilitate the offshore continuum for coastal applications. Consequently, the AGRIF software has been introduced into a coastal numerical model, namely MARS3D (Lazure and Dumas, 2008). The two-way nesting is now fully operational for mass and momentum

60 conservation. Implemented along the coasts of the north western European shelf and over coastal bays, the mesh refinement should allow the representation of a large spectrum of spatial (small bays and large areas) and temporal (fast as tides or and surges and slow as mesoscale or frontal instabilities) scales.

This paper aims to demonstrate the capabilities and benefits of the two-way nesting method for the modelling of the interplay of coastal and regional dynamics. Section 2 describes the recent developments in the hydrodynamic model MARS3D with

65 AGRIF library, and the running performance are addressed. Afterwards two applications are presented. In Sect. 3, a regional

modelized configuration is depicted and focused on the systematic refinement capability. In Sect. 4, a focus coastal configuration is introduced to highlight two-way nesting improvements. Finally, these results are discussed and futures perspectives are given in Sect. 5.

2. Innovative developments for two-way nesting

2.1. The MARS3D model (V11.2 released in March 2018)

The hydrodynamic MARS3D (Model for Applications at Regional Scale) model solves the primitive equations under the Boussinesq and hydrostatic assumptions. It uses finite differences over a staggered Arakawa C-grid with a vertical sigma coordinate framework. MARS3D V6 is fully described in Lazure and Dumas (2008). It relies on a mode barotropic / baroclinic splitting. The barotropic mode, which obeys the shallow water equation systems, is treated with a modified Alternating Direction Implicit (ADI) algorithm. Contrary to split explicit free surface models and due to the wider range of stability of the barotropic mode, the temporal integration of both modes is carried out with the same time step which on the one hand simplifies the barotropic/baroclinic coupling but on the other hand filters the barotropic mode weaker as long as the numerical filter is implicit rather than explicit. The original ADI algorithm (Leendertse and Gritton, 1971) has been significantly modified by first adding a prediction step (assessment of $v^{n+1,*}$) and then by alternating the sweep of the computational grid in a row-column-wise manner and in a column-row-wise manner. These modifications were introduced to limit the spatial split errors inherent to single time step schemes. The row-column wise manner is developed in Eq. (1): it consists in computing $(u^{n+1}, \eta^{n+1,*})$ in the first step and then (v^{n+1}, η^{n+1}). The second half time step which gives in a symmetric manner firstly $(v^{n+1}, \eta^{n+1,*})$ then (u^{n+1}, η^{n+1}) is not detailed. The first equation of the system is a local solver whereas the second and the third equations solved together lead to a linear tridiagonal system which size is twice the number of grid cells in row because the unknown vector is made of $(u^{n+1}, \eta^{n+1,*})$. Similarly, the fourth and fifth equations lead to a linear tridiagonal system which size is twice the number of points in column.

$$v^{n+1,*} = v^n - g\Delta t \frac{\partial \eta^n}{\partial y} + \Delta t G_v(u^{n-1}, v^{n-1})$$

$$\eta^{n+1,*} = \eta^n - \Delta t \left[\frac{\partial}{\partial x}(h^n u^{n+1}) + \frac{\partial}{\partial y}(h^n v^{n+1,*}) \right]$$

$$u^{n+1} = u^n - g\Delta t \frac{\partial}{\partial x}(\alpha \eta^n + (1-\alpha)\eta^{n+1,*}) + \Delta t G_u(u^n, v^n)$$

$$\eta^{n+1} = \eta^n - \Delta t \left[\frac{\partial}{\partial x}(h^n u^{n+1}) + \frac{\partial}{\partial y}(h^n v^{n+1}) \right]$$

$$v^{n+1} = v^n - g\Delta t \frac{\partial}{\partial x}(\alpha \eta^n + (1-\alpha)\eta^{n+1}) + \Delta t G_v(u^n, v^n) \tag{1}$$

In the Eq. (1), h stands for the total water depth, Δt is the time step and α is the implicit coefficient of the external pressure gradient term. The term $G_{u/v}(u^n, v^n)$ gathers the vertical average of all the remaining terms including the non-linear and the

horizontal dissipation terms, the Coriolis force, the friction at the surface and the bottom. All of these last ones are explicit and

95   not discussed here.

In a context of massive parallel computation, these equations are solved using a decomposition domain into horizontal tiles. The main drawback of the ADI is its non-local solver for a given row (second and third gathered equations of Eq. (1)) which elements are distributed on the various tiles crossed by the row considered. The solver consists of a linear system which coefficients are distributed on various tiles. The linear system associated to Fig. 1 can be schematically written as diagonal

100   blocks linear system where each block is itself tridiagonal:

$$\begin{pmatrix} coef\ on\ tile\ 1 & \cdots & 0 \\ \vdots & \ddots & \vdots \\ 0 & \cdots & coef\ on\ tile\ n \end{pmatrix} \begin{pmatrix} \eta, u\ on\ tile\ 1 \\ \vdots \\ \eta, u\ on\ tile\ n \end{pmatrix} = \begin{pmatrix} rhs\ on\ tile\ 1 \\ \vdots \\ rhs\ on\ tile\ n \end{pmatrix} \tag{2}$$

It clearly raised the question of gathering the linear system on a single tile to solve it and the broadcast the solution (vector made of the (u, η) for the whole row) from the single tile used for the solver to each appropriate geographic tile. It induces a wide set of MPI messages commensurable with twice the size of the row. In order to reduce by a factor of two the

105   communications, the first three equations of the system (1) were rearranged into the system (3) thanks to the splitting of u^{n+1} into an explicit part and an implicit one. This leads to a tridiagonal system which unknown vector is made solely of $\eta_i^{n+1,*}$. Therefore, for a given row j, the size is exactly the number of grid cells in the x-direction instead of twice this size for the regular ADI algorithm for which unknown vectors are made of $\eta_i^{n+1,*}$ and u_i^{n+1}. Thus, it reduces the size of the data involved in the message passing interface between tiles by a factor of 2.

110
$$v^{n+1,*} = v^n - g\Delta t \frac{\partial \eta^n}{\partial y} + \Delta t G_v(u^{n-1}, v^{n-1})$$

$$u^{n+1,*} = u^n - g\Delta t \alpha \frac{\partial \eta^n}{\partial x} + \Delta t G_u(u^n, v^n)$$

$$-g\Delta t^2(1-\alpha)\frac{\partial}{\partial x}\left[h^n \frac{\partial \eta^{n+1,*}}{\partial x}\right] + \eta^{n+1,*} = \eta^n - \Delta t \left[\frac{\partial}{\partial x}(h^n u^{n+1,*}) + \frac{\partial}{\partial y}(h^n v^{n+1,*})\right]$$

$$u^{n+1} = u^{n+1,*} - g\Delta t(1-\alpha)\frac{\partial \eta^{n+1,*}}{\partial x} \tag{3}$$

Besides the modification of the barotropic solver itself, some additional modifications were performed in the

115   barotropic/baroclinic coupling. The original iterative coupling described by Lazure and Dumas (2008) which was designed for the Eq. (1) has been abandoned as it was not compatible anymore with the reformulation (3). The coupling that can be sketched according to Fig. 2 is not iterative anymore to get a convergence of the coupling terms. It is now straightforward: (a) the barotropic mode being forced with vertically integrated terms of advection, horizontal dissipation, Coriolis, internal pressure gradient and the bottom friction (assessed with the first level of horizontal velocity); (b) the baroclinic mode is forced with the

120   external pressure gradient; (c) The last classical step of the coupling consists in redistributing the vertical misfit between the barotropic transport and the vertically integrated baroclinic transport in order to render them both compatible with the conservation equation and preserve the mass.

4

Last but not least, the drying and flooding capability has been modified in order to introduce partially drying or wetting. It consists in introducing in the non-local continuity equation a reduction coefficient hereafter noted f_{wet} for partially dried cells into Eq. (4):

$$\eta^{n+1}Sf_{wet}^{n+1} = \eta^n Sf_{wet}^n - \Delta t\left[\partial_x(h^n u^{n+1})\Delta y + \partial_y(h^n v^{n+1})\Delta x\right] \tag{4}$$

where S stands for the grid cell surface ($S = \Delta x \Delta y$) and f_{wet} is the time-dependent fraction of the grid cell which is flooded ($0 \leq f_{wet_{i,j}} \leq 1$). f_{wet} is given by a prognostic equation accounting for the bottom slope within the grid cell and the water column height at its centre.

2.2. The AGRIF library: Mesh refinement and grid interactions

AGRIF (Adaptive Grid Refinement In Fortran from Debreu et al. (2008)) is a package for the integration of Structured Adaptive Mesh Refinement (SAMR) features within a multidimensional finite difference model. Its main objective is to simplify the integration of SAMR potentialities within an existing model, whilst making minimal changes. In particular, it includes a lexicographic analyser of Fortran code that generates, at the compilation step, the data structures required for running the same code on any grid hierarchy. AGRIF is currently used in the following ocean models: ROMS-AGRIF (Debreu et al., 2012; Penven et al., 2006) a regional model developed jointly at Rutgers and UCLA universities; NEMO ocean modelling system (Biastoch et al., 2018, 2009) a general circulation model used by the European scientific and operational communities; and HYCOM a regional model developed jointly by the University of Miami and the French Navy. For MARS3D model, a first implementation was introduced to assure the mass conservation with one-way nesting (Muller et al., 2009) and in two-way nesting only for temperature and salinity (Dufois et al., 2014). The two-ways nesting is now fully operational for mass and momentum conservation taking into account intertidal areas.

2.2.1. General algorithm

For a general review of two-way nesting algorithms, the reader is referred to Debreu and Blayo (2008). This section overviews the general algorithm introduced in MARS3D characterized as a split implicit free surface model. Figure 3 illustrates two child grids covering subdomains ω of the parent domain Ω and their boundaries are delimited by the interfaces Γ. The coarse resolution grid has a mesh size given by Δx_H, while the fine resolution grid has a mesh size $\Delta x_h = \Delta x_H/\rho$ where ρ is the spatial mesh refinement ratio (it is an integer). Subscripts H and h stand respectively for the coarse and the refined domains. The partial differential equations solved by the model are written in the following generic form:

$$\frac{\partial q}{\partial t} = L(q) \tag{5}$$

They are integrated from an initial state and with lateral open boundary conditions prescribed at the limits of Ω. These equations are discretized on the coarse (H) and fine (h) grid domains by:

$$\frac{\partial q_H}{\partial t} = L_H(q_H), \qquad \frac{\partial q_h}{\partial t} = L_h(q_h) \tag{6}$$

Thus L_H and L_h are the discretizations of the same continuous operator L at different resolutions. The child grid lateral boundary conditions at the interface Γ are provided by temporal and spatial conservative interpolations from the coarse grids. In two-way mode, the coarse solution is updated using the fine solution once the temporal integration of the fine grids is completed. This is modelled by two different operators: a spatio-temporal interpolator (P) and a restriction operator (R) respectively. Assuming that the model is fully explicit, the algorithm can be written in the following conceptual form for a single time step of the coarse grid:

(1) $q_H^{n+1} = L_H(q_H^n)$ (Temporal integration of the coarse grid)

(2) For $m = 1 \ldots \rho_t$ Do

$$\left. q_h^{n+\frac{m}{\rho_t}} \right|_\Gamma = P(q_H^n, q_H^{n+1}) \text{ (Computation of Open Boundary Conditions from the coarse grid to the child grid)}$$

$$q_h^{n+\frac{m}{\rho_t}} = L_h\left(q_h^{n+\frac{(m-1)}{\rho_t}}\right) \text{ (Temporal integration of the child grid)}$$

(3) $q_H^{n+1}|_\omega = R(q_h^{n+1})$ (Update of the coarse grid over the area of overlapping)   (7)

Here, ρ_t is the time refinement factor ($\rho_t = \Delta t_H / \Delta t_h$) which is equal to the space refinement factor ρ if the model is restricted to a CFL (Courant Friedrichs Levy) stability condition. The step (1) corresponds to the integration of the coarse grid model for one time step Δt_H on Ω, while the step (2) corresponds to the integration of the fine grid model over ρ_t time steps. The interpolator P makes use of q_H^n and q_H^{n+1} to produce space and time interpolations on the interface Γ.

2.2.2. Open Boundary Conditions

At the boundaries of the subdomains, the mother grid provides the high-resolution grids with the free surface, tracers and barotropic and baroclinic velocity components. Due to the arrangement of the grids along the Γ interface, these open boundary conditions require bidimensional interpolation as long as the first external (*i.e.*, not-computed) fine grid points (u, v or η) used for open boundary conditions do not coincide with any coarse grid point. These variables are interpolated onto the fine grid by combining Piecewise Parabolic Method (in the normal direction to the boundary) and linear method (in the along direction to the boundary). Afterwards the open boundary conditions (caracteristics or radiation methods respectively for momentum and tracer) are computed to force the fine grid. In that sense the various fluxes entering the fine grid are not the ones that output from the coarse grid. Thus, the conservation of the global system (coarse grid plus fine grids) is reached thanks to the update step (see Sect. 2.2.3).

In addition, a sponge layer is set along the open boundaries. As explained in Debreu and Blayo (2008), the sponge layer is implemented as a diffusion term that acts on the difference between the high-resolution solution and the interpolation of the coarse resolution solution on the fine grid:

$$\frac{\partial q_h}{\partial t} = L_h + \nabla \cdot \left(\mu \nabla (q_h - I_H^h q_H) \right) \tag{8}$$

where μ is a coefficient ranging from its maximal value μ_0 at the interface to 0 a few grid points away from it (usually at a distance of 3 coarse grid cells). This sponge layer is applied both on momentum and tracers. It aims at filtering out scales that are not affordable by the coarse grid and to get a better match in term of scales between the open conditions (coming out from the coarse grid) and the state variable q_h at first inner points along the open boundary conditions of the fine grid which come out from the operator L_h which spectral range is wider.

2.2.3. Free surface, tracer and velocity updates with wetting and drying

After the time integration of the high-resolution grids, the information is fed back to the parent grid in the two-way context: the updated coarse solution becomes the spatial average of the fine solution. In order for this restriction operator (R) to keep the fluxes coherent and conserve mass, the mother and child bathymetries have been constructed so that the bathymetry reduction conserves volume. Contrary to split explicit models for which a limited updated area next to the boundary of overlapping is required, the semi-implicit solver used in Mars require to update the full area of overlapping as long as the barotropic solver is not local (but across the full domain).

In a free surface ocean model, for conservation reasons, the discrete time evolution of the free surface elevation can be written in terms of the divergence of the barotropic transports U and V in the x and y directions (volumetric fluxes):

$$S_{i,j} f_{wet_{i,j}}^{n+1} \eta_{i,j}^{n+1} = S_{i,j} f_{wet_{i,j}}^{n} \eta_{i,j}^{n} - \Delta t \left[U_{i+\frac{1}{2},j} - U_{i-\frac{1}{2},j} + V_{i,j+\frac{1}{2}} - V_{i,j-\frac{1}{2}} \right] \tag{9}$$

A consistent update scheme for free surface and barotropic transport has be obtained by applying the restriction operator to the right-hand side of this equation. Hereafter, one considers the situation represented in Fig. 4 where the mesh refinement coefficient is equal to 3. The free surface restriction operator is a simple average of the 9 fine grid cells (and assuming there is no time refinement) using the following area weighted formulae:

$$S_{i_c,j_c} f_{wet_{i_c,j_c}}^{n+1} \eta_{i_c,j_c}^{n+1} = \sum_{\substack{i=i_f-1,i_f+1 \\ j=j_f-1,j_f+1}} S_{i,j} f_{wet_{i,j}}^{n+1} \eta_{i,j}^{n+1} \tag{10}$$

where i_c and j_c are the indices of the cell in the coarse grid and i_f and j_f in the fine grid (see Fig. 4). Using Eq. (9), the time evolution of the updated free surface is given by:

$$S_{i_c,j_c} f_{wet_{i_c,j_c}}^{n+1} \eta_{i_c,j_c}^{n+1} = S_{i_c,j_c} f_{wet_{i_c,j_c}}^{n} \eta_{i_c,j_c}^{n} - \Delta t \left[\begin{array}{l} \left(U_{i_f+\frac{3}{2},j_f-1} + U_{i_f+\frac{3}{2},j_f} + U_{i_f+\frac{3}{2},j_f+1} \right) - \left(U_{i_f-\frac{3}{2},j_f-1} + U_{i_f-\frac{3}{2},j_f} + U_{i_f-\frac{3}{2},j_f+1} \right) \\ + \left(V_{i_f-1,j_f+\frac{3}{2}} + V_{i_f,j_f+\frac{3}{2}} + V_{i_f+1,j_f+\frac{3}{2}} \right) - \left(V_{i_f-1,j_f-\frac{3}{2}} + V_{i_f,j_f-\frac{3}{2}} + V_{i_f+1,j_f-\frac{3}{2}} \right) \end{array} \right] \tag{11}$$

Consistently with the average restriction operator for the free surface, the coarse grid barotropic transports can then be updated by the relations:

$$U_{i_c+\frac{1}{2},j_c} = U_{i_f+\frac{3}{2},j_f-1} + U_{i_f+\frac{3}{2},j_f} + U_{i_f+\frac{3}{2},j_f+1}$$

$$V_{i_c,j_c+\frac{1}{2}} = V_{i_f-1,j_f+\frac{3}{2}} + V_{i_f,j_f+\frac{3}{2}} + V_{i_f+1,j_f+\frac{3}{2}} \tag{12}$$

This corresponds for U to an injection in the x−direction and an average in the y−direction and reciprocally for V. As time refinement is applied, these fluxes have been summed up over the ρ_t fine grid time steps.

Another crucial point is that the free surface update using Eq. (10) must preserve constancy: if the fine grid free surface η is spatially constant, the update operator has to preserve this constant. In MARS3D, this is achieved by updating the wet fractions of the coarse grid according to:

$$f_{wet_{ic,jc}}^{n+1} = \frac{1}{S_{ic,jc}} \sum_{\substack{i=i_f-1,i_f+1 \\ j=j_f-1,j_f+1}} S_{i,j} f_{wet_{i,j}}^{n+1} \tag{13}$$

Moreover, in order to keep constancy preservation, tracer values must be updated with the same update operator as for the free surface. The three-dimensional velocities (or more precisely volumetric fluxes) must also be updated with the same update operator as for the barotropic velocities. Thus, this updated process gives a global mass (water, tracers, …) conservation of the system which is the mass contained in the coarse grid outside of the fine grid overlapping areas plus the mass contained in all the fine grids.

2.2.4. Interactions between child grids

In that new release of MARS3D-AGRIF system, we enable exchange of information at same hierarchical grid level thanks to a modified update procedure that allow the information from one child grid to another to travel through the mother grid. It requires an overlapping area between child grids of same hierarchical level. After the numerical integration of each grid, their fields are weighted on the overlap area to update the parent grid. The weights are estimated once and for all during the pre-processing phase. For each sub-cell of a coarse cell, these weights are computed to favor(/disfavor) a child grid information over another if its sub-cell is further from (/closer to) the open boundary. Thus, child grids get the same shared information along their boundaries of the overlapping areas. This concerns all the state variable fields: the sea surface elevation, currents, temperature, salinity and any additional tracers. The recommended size of the overlap area in one direction is at least three times the spatial refinement factor. Figure 3 illustrates the weight distribution between two child grids at the same hierarchical level on the overlap area represented by the red rectangle.

This functionality is only available with a single zoom level so far. It is a major issue that need to be address for multiple level hierarchy approach. This constraint will be coped within the next upgrade of AGRIF library to be portable into any numerical models.

2.3. Parallelization option

The MARS3D model and the AGRIF library can be run with either sequential mode, OMP mode, MPI mode or hybrid mode (based on both MPI and OMP parallelization). The OMP method is based on classical Fine-Grain approach where OMP directives share the work between threads, in particular at the level of parallel loops with the DO directive. In order to avoid overhead of work sharing and creating/managing threads, the parallelization is done on the j column loop. For the MPI mode,

8

an optimized domain decomposition is defined before the run to balance the load on the different cores of the cluster. It consists in attributing to each MPI rank approximately the same number of wet grid cells and excluding the land-masked part of the domain. The hybrid computation is based on both MPI (domain decomposition) and OMP (distribution of threads in Fortran loops inside each MPI domain) parallelization. It has been implemented following the MPI_THREAD_FUNNELED type where MPI calls are only made outside of OMP parallel regions.

For a unique child per level nesting configuration, mother and child grids are resolved sequentially with the same parallelization option. To facilitate the distribution of cores, it is thus recommended to work with grids of rather the same numbers of mesh. In the case of multiple child grids at the same level, the user can choose between two possibilities for the integration of the child grids: sequentially or simultaneously. The first solution consists in a sequential integration with the same number of processors for each child grid; The second solution involves a distribution of the MPI ranks among all child grids. For this latter, the ranks are allocated to the child grids at the beginning of the simulation, based on the number of wetting cells in every child grid. In this way, ranks can be assigned between all child grids or within multiple groups of child grids on the same hierarchical level. This last option is favorable when the size of child grids differs from one another or when the child grids are much smaller than the mother grid.

2.4. Computational cost

To evaluate the performance of this implementation, several tests were performed with two different configurations presented in next sections with classical offline one-way nesting ang two-way nesting. First, the coarser model has been run independently over the whole computation period to get information to force the child grid area at hourly frequency. Baroclinic currents, temperature and salinity variables are then interpolated horizontally and vertically onto the child grid with an external homemade Fortran tool. For the regional configuration composed normally of seven child grids, only the one focused on the Iroise sea (see Fig. 5) was kept for the purpose of this experiment.

The computational times for the simulation of 45 days are provided in the Table 1 for both MARS3D one-way classical offline nesting or MARS3D/AGRIF two-way nesting. All the simulations have been performed on the supercomputer DATARMOR infrastructure, composed of 396 nodes with 28 cores each (https://wwz.ifremer.fr/pcdm). Since the computing performance depends on the load of the machine, the computational cost has been evaluated from a pool of repeated experiments (five times). For each configuration, the different models (one-way and two-way) have been run with the same parallelized discretization but with two different parallelization methods: a classic MPI domain decomposition and a hybrid computation based on both MPI (domain decomposition) and OMP (distribution of threads in Fortran loops inside each MPI domain) parallelization.

Table 1: Mean computation time given in hours for both modelized configurations for a simulation of 45 days.

Configuration	Mode	Cores	Distribution	Scenario	one-way offline	two-way online

9

Regional	MPI	56	56 MPI ranks	Hydrodynamic only	12.0	15.0
Coastal	MPI	112	112 MPI ranks	Hydrodynamic only	13.5	18.6
Regional	Hybrid	448	56 MPI ranks with 8 OMP threads each	Hydrodynamic only	2.9	4.3
Coastal	Hybrid	336	48 MPI ranks with 7 OMP threads each	Hydrodynamic & 13 passive tracers	21.1	29.2

For both configurations, the computation time is increased by one third for the AGRIF configuration compared to the classical offline one-way nesting. This difference is explained with the constant spatial interpolation performed within the AGRIF library at each fine grid time step. The update process which assures the fluxes continuity, covers the fine grid area in the coarse grid and is also responsible for this increase. For the one-way nesting chain, the handling time of 3D output files and the waiting time due to DATARMOR load activity have not been taking into account. Their introduction would decrease the whole difference especially if several zooms are implemented.

As shown with the regional example, using hybrid parallelization with 8 times more computational resources than with MPI decreases the total time by a ratio 4. This last solution is an efficient way to require more resources without having to consider domain decomposition in complex geographic areas. The advection-diffusion evolution of 13 passive tracers in the coastal configuration is another example where hybrid mode makes it possible to achieve reasonable calculation times.

3. Systematic refinement of the coastal zone: Paving the French Atlantic coast within a regional configuration

3.1. Bay of Biscay configuration

The MARS3D model has already been used to investigate the Bay of Biscay and its extension to the western English Channel (Huret et al., 2013; Lazure et al., 2009). Here, the MARS3D/AGRIF capability is implemented along the North-Western European continental shelf. Figure 5 shows how the AGRIF skill is used to pave the coast line from Spain to Belgium with overlapping grids. Seven zooms with a resolution of 500m and roughly the same grid size are introduced into a coarser 2.5 km resolution grid that encompasses all the seven grids. The coarser grid is itself included in a larger 2D model (5km resolution) in which the tide is imposed using the FES 2014 ocean tide atlas with 14 harmonics constituents (Lyard et al., 2021). The 3D open boundary conditions for temperature and salinity of the coarser grid are provided at a daily frequency with the MERCATOR PSY2V4 re-analysis model. The main hydrological runoffs are set in the zooms (96 rivers accounted for) from different source databases (Spain, English, French and Netherlands). The atmospheric forcings are picked up in the Météo France ARPEGE High Resolution (0.1°) analysis with hourly data for the coarser grids. For the child grids, the atmospheric forcings rely on the Météo France AROME (2.5 km) analysis with hourly data. The discretisation over the vertical axis is performed with 40 generalized σ-layers with a stretching function that induces refinement above 150m depth, next to the surface. A space refinement factor of 5 is used between each grid level but the time refinement is adapted according to the

10

295 maximum velocity encountered locally. Thus, the time refinement coefficient is heterogenous: it is either 3 (over areas with rather slow flows) or 5 (in very energetic areas such as in the middle of the English Channel). In the same way, the horizontal turbulent closure consists of a Laplacian operator with a constant turbulent viscosity coefficient which differs between each zoom ranging from 0.5 up to 3 $m^2.s^{-1}$.

Two realistic hindcasts have been realized over several years (2010-2019 for the two-way and 2017-2018 for the one-way) to
300 demonstrate and characterize nesting benefits. For each hindcast, a spin-up of 3 months has been performed. These two common years have been selected upon the available datasets for several validation parameters detailed in appendix A.

3.2. Hydrodynamic impact over open boundary conditions

The ongoing issue for nesting models relies on open boundary conditions. For the AGRIF configuration, the tidal propagation is performed using sea surface elevation and fluxes interpolation. For the regional Bay of Biscay configuration, the initial tide
305 forcing is imposed at the mother grid's boundary with FES model, composed of 12 tidal harmonic components. A zero gradient condition is applied to currents. To force the child grid in classic one-way nesting, the SHOM CST-France model is normally used as it contains 112 components and a Dirichlet boundary conditions is applied for currents. This tidal model has been accurately validated throughout the French tidal gauge network RONIM.

The modelled tidal signal is compared to hourly validated data from four tidal gauge available in the studied area. The main
310 statistics are estimated over one year are given in the Table 2 for the regional Bay of Biscay configuration. The tide from the two-way techniques is slightly less precise than the one-way simulation. This occurs especially at the north-eastern boundary, at Roscoff, where the RMSE is twice as large. On the opposite at the southern boundary, at Concarneau, the differences are in favour of the two-way nesting.).

Table 2: Comparison of sea surface elevation between MARS3D one-way (normal font) and MARS3D/AGRIF two-way (bold font)
315 **for the Iroise zoom (500m horizontal resolution) compare to RONIM tidal gauges.**

	Roscoff	Le Conquet	Brest	Concarneau
Normalize standard deviation (%)	1.022 **0.969**	1.010 **1.004**	0.988 **0.990**	1.029 **1.024**
Root mean square error (cm)	9.3 **18.7**	7.2 **9.4**	10.5 **12.2**	7.9 **6.4**
Pearson correlation coefficient (%)	0.999 **0.985**	0.999 **0.993**	0.998 **0.990**	0.998 **0.995**

To observe the influence of the tide propagation, the nested configuration has been compared to the PREVIMER harmonic component atlas with the zoom grids. This atlas has been built upon a series of barotropic simulations at 250m horizontal resolution and validated with the RONIM network (Pineau-Guillou, 2013). A harmonic decomposition has been applied to

11

320   each hindcast with an hourly output frequency over a period of one year. In Table 3, a comparison of wave elevations is given for the waves M2, S2, O1, K1 at 4 different points distributed in the Iroise sea. Both models are in rather good agreement with the reference atlas. The main difference is found for the MARS3D/AGRIF two-way configuration for the K1 wave on relative difference, where the wave errors are over estimated by 20%, but the difference is less than 2 cm.

Table 3: Comparison of wave elevation amplitudes between MARS3D one-way (normal font) and MARS3D/AGRIF two-way (bold
325 **font) for the Iroise zoom (500m horizontal resolution). The model amplitudes are given in cm with the relative difference between model and observation in %.**

	M2	S2	O1	K1
Point 1	201.3 (-3%)	73.4 (-2%)	7.0 (+9%)	7.5 (+9%)
5.27°W - 48.7°N	**198.8 (-4%)**	**74.0 (-1%)**	**6.0 (-2%)**	**8.8 (+29%)**
Point 2	169.2 (-1%)	63.8 (-1%)	7.0 (+6%)	7.0 (+5%)
5.27°W - 48.48°N	**170.3 (-1%)**	**63.0 (-1%)**	**6.4 (-1%)**	**8.4 (+27%)**
Point 3	179.1 (-2%)	65.6 (-2%)	7.0 (+9%)	7.0 (+13%)
5.5°W - 48.3°N	**180.0 (-2%)**	**66.51 (-1%)**	**6.5 (-2%)**	**8.5 (+36%)**
Point 4	192.2 (-2%)	72.1 (-1%)	7.0 (+5%)	7.3 (+5%)
4.7°W - 48.3°N	**192.3 (-2%)**	**72.3 (-1%)**	**6.0 (-6%)**	**8.4 (+21%)**

    This comparison has been also done for the barotropic currents. The differences between both models are higher for the minor waves O1 and K1 with difference of 5 cm.s^{-1} and relative difference of 30% for some points. However, the validation of the
330 PREVIMER atlas currents was not available all over the area due to a lack of long time series data over the French coast. In the same idea, barotropic currents have been compared to different available ADCP datasets that were recorded in the Bay of Brest or in Molène archipelago. As they are mainly situated over shallow waters, there have been no significant difference between nesting techniques.

3.3. Hydrologic validation

335 A detailed qualification of the regional Bay of Biscay configuration has been done (Bezaud and Pineau-Guillou, 2015). It has highlighted the enhancements of predictions with increasing resolution in the coastal areas where the 500m zoom models have been implemented. These comparisons have been made against coarser models and the conclusions may therefore seem obvious. Indeed, a finer resolution allows the model to simulate accurately the small-scale structures (instabilities of the front, eddies, filaments...).

340 Here, an evaluation of the two-way nesting versus one-way nesting at the same horizontal scale is performed over a two-year period from 2018 to 2019. The evaluation focuses on the Iroise Sea zoom with different mooring stations (see black points in Fig. 5 and Fig. 8). Figure 6 displays a Taylor diagram for temperature (Fig. 6a) or salinity (Fig. 6b) and another diagram

that represents bias values and root mean squared errors (RMSE). These graphs summarize the comparisons between the available datasets (see appendix A) and both nesting methods. It appears that the nesting impact is not homogenous over the whole domain.

First, the two-way nesting technique improves the overall performance of the model compared to oceanic datasets (see green points for one-way and yellow points for two-way). The simulated temperature offsets are noticeably reduced. The main favourable impact is the drop of the root mean square error by 0.4°C for the COAST-HF MAREL Iroise point. For salinity comparisons, the RMSE and the bias exhibit to be in the same order of magnitude. The major improvement relies on the enhancement of correlation for the COAST-HF ASTAN dataset. This could be due to the vicinity of this point to the eastern border of the zoom. The update ability of AGRIF two-way enables more realistic incoming fluxes at high temporal resolution. The relative standard deviation of the simulated salinity at MAREL Iroise buoy is also considerably reduced. As this point is located in the strait of Brest, the tidal variations of salinity front are somehow better simulated for the same reason.

3.4. Focus on particular processes

In the Iroise Sea during the summer, the Ushant front is depicted by cold water of about 14°C. Over shallow depths, the tidal currents are intensified and very strong around Ushant and Molène archipelago. The induced tidal stirring is so large that waters are mixed (and homogeneous) from the sea surface to the bottom. Further offshore, the summer stratification can develop and the sea surface is clearly warmer (above 18°C). This phenomenon can be seen on satellite data on Fig. 7 for the 15 of August 2016 for both Landsat 8 (Fig. 7a) and ODYSSEA (Fig. 7b) products described in appendix A. Compare to ODYSSEA, the Landsat surface temperature is overestimated in different spots near the coast, in the bay of Brest for example with values over 20°C which might be due to mis-flagged clouds.

The ability of the two-way nesting approach (Fig. 7d) to correctly reproduce this spatial feature is clear while the one-way nesting (Fig. 7c) struggles to simulate this phenomenon. Indeed, the Ushant front is nearly missing in the one-way simulation and is much better characterized in the two-way simulation at 5.25°W. The temperature magnitudes are strengthened on each side of the front thanks to the AGRIF update. Furthermore, this improvement supports the realism of the fine structures around the shoals of Sein Island and in the Molène archipelago in the two-way simulation. On another hand, one could notice the open boundary effect in the south part of the one-way simulation where an east-west temperature front is created. An upwind scheme is prescribed to temperature and salinity when using one-way nesting (*i.e.,* apply external value when the water mass enters the domain).

For wide open areas such as Iroise Sea, the benefit of the feedback/update of the zoom contributes to the correct representation of the thermic Ushant front mainly by enlarging the span of scale captured (*e.g.,* fine eddies and filaments), which is expected, but also in term of the horizonal localisation of thermal front, which is less expected. As a matter of fact, the forcing through the open boundaries is of primary importance for limited area models; it may dramatically impact the local coastal processes, even in areas where the dynamics is highly controlled by large scales such as the tidal forcing. Even if the tidal signal is better represented with the one-way nesting (due to the CST-France model), the upwind scheme applied for tracers at open boundaries

is not sufficient for the heat exchange at an hour frequency. The chosen simulated domain is not large enough with one-way nesting to get a sharp temperature front.

4. Highlighting the benefit of a two-way conservative approach: Estimating renewal time over a coastal area

4.1 Bay of Brest configuration

380 The Bay of Brest is a semi-enclosed macrotidal ecosystem is located at the western end of Brittany (France), spanning over 180 km^2. It is connected to the Iroise Sea through a 1.8-km wide by 6-km long and roughly 50-m deep inlet (called the Goulet de Brest). The strong hydrodynamic currents due to its complex geometry and topography are relatively well known, being the purpose of many previous studies. This macro-tidal coastal area is characterised by a dominant semi-diurnal tide with a tidal range of 1.2 to 7.3 m. The tidal currents peak up to 3 m s^{-1} in the Goulet and are in quadrature phase relative to the surface

385 elevation (Petton et al., 2020). The mean volume at mid-tide inside the bay is roughly 2 billion m^3. As its average depth is only of 8 m, the back-and-forth flow at each tide prevents stratification nearly everywhere (Le Pape and Menesguen, 1997). The tidal prism is 25% of the mean volume in neap tide and 60% in spring tide. The hydrology is dominated by freshwater runoffs coming mostly from the Aulne river (Auffret, 1983). The atmospheric forcings rely on the Météo France AROME (2.5 km) analysis with hourly data.

390 The MARS3D/AGRIF model is set up over the Iroise sea (geographic limits 47.74°N - 48.82°N and 4.08°W - 5.55°W) with a horizontal grid resolution of 250m. A zoom over the Bay of Brest is introduced with a resolution of 50m (geographic limits 48.20°N - 48.44°N and 4.09°W - 4.72°W), see Fig. 8. The time and space refinement factors are both equal to 5. The vertical discretization is performed with 20 equidistant σ-layers in both grids. The bathymetries are interpolated from a combination of different digital terrain models (SHOM, Ifremer, IGN). The Iroise model is forced by harmonic components from the SHOM

395 CST-France model (Le Roy and Simon, 2003). The 3D open boundary conditions for baroclinic currents, temperature and salinity are imposed at hourly frequency from a hindcast of the previous regional configuration (Inter annual hydrodynamic hindcast with MARS3D-AGRIF model - Bay of biscay and Manche Areas). Freshwater inputs for the four main rivers in the Bay have been taken from the French HYDRO database (http://www.hydro.eaufrance.fr/) and corrected with corresponding watershed surface rates. The configuration is available with a more detailed description of physical, numerical and

400 parallelisation parametrisations from Petton and Dumas (2022).

4.2. Hydrologic validation

Two realistic hindcasts have been realized over 2017 up to 2019 for both one-way and two-way nesting techniques. The coastal Bay of Brest one-way configuration has already been validated in detail in previous studies (Petton et al., 2020; Frère et al., 2017). The two-way nesting has the same ability to reproduce the main characteristics of currents and water elevation with a

405 high level of realism, so the comparisons are not shown. However, some differences are observed in the temperature and salinity predictions. As previously stated, the one-way nesting solution is already in good agreements with the dataset (see

14

blue points for one-way and red points for two-way in Fig. 6). It is explained by the parametrisation performed with the bottom drag coefficient spatialisation and the vertical turbulence closure. It is also due to the fact that the flows are driven by the tide whose large-scale features are easily captured (Petton et al., 2020) in this semi-enclosed area. Its relatively shallow depth along with highly variable turbulent mixing make the dynamics less sensitive to boundary effects. The two-way nesting technique barely enhances the performance of the model. For temperature, the main improvement is the reduction of bias. This could be explained by the nesting feedback that enables a more accurate global temperature budget in the mother grid. Here again, the simulated domain could have been larger to override this issue pushing the boundaries away from the Iroise sea. For salinity, the model also reduces the relative standard deviation for the MAREL Iroise and ECOSCOPA datasets. As the water runoffs are identical, this amelioration might be hard to explain. It may result in a better simulation of current flows with nonlinear effects.

4.2. Timescale indicator

As the shallow ocean is subject to large environmental and anthropogenic pressures, the fate of coastal waters is a key for environmental, ecological and economic issues. Therefore, global and local indicators are crucial for stakeholders to anticipate the spill of different types of materials such as oil (Jordi et al., 2006) or micro-plastics (Frère et al., 2017), biogeochemical processes due to nutrients flushing (Le Pape and Menesguen, 1997; Fiandrino et al., 2017), pollution phenomena (Jiang et al., 2017; Neal, 1966) or to develop restoration solutions (Kininmonth et al., 2010; Rossi et al., 2014; Thomas et al., 2014).

There are numerous indicators of hydrological characteristics based on theories of transport timescales. Over the years, many studies (Bolin and Rodhe, 1973; Zimmerman, 1976; Monsen et al., 2002; Takeoka, 1984) have defined and assessed different scales to describe water renewal on a particular spatial scale (a bay, an estuary, a harbour) in which mixing processes will renew the water mass (through open-ocean–connected boundaries or forced by runoff inputs). However, the vocabulary remains very diverse (Bacher et al., 2016). Those time scales are often provided in the framework of the constituent-oriented age and residence time theory (CART, www.climate.be/cart), under different names depending on their exact purpose (Deleersnijder et al., 2001; Delhez, 2006; Delhez et al., 2004; de Brauwere et al., 2011). They can also be used to specify the transport in the vertical direction (Meier, 2005; White, 2007; Bendtsen et al., 2009). Lucas and Deleersnijder (2020) have made a specific review of the whole set of indicators estimated either with Eulerian method or Lagrangian computation with particle-tracking. Most of these timescales can be averaged over the whole basin or can be defined locally, at every position in the basin, to provide a more detailed spatially distributed information on the water renewal capacity of a basin (Jouon et al., 2006). Moreover, under certain physical circumstances (large diffusion processes and weak runoffs), they can be identical (Viero and Defina, 2016b).

Our intent is not to debate the pros and cons of the different indicators that exist and the way they are computed. Here, the goal is to highlight the two-way nesting capabilities for characterizing the renewal process of the Bay of Brest. Therefore, the *e*-folding flushing time is evaluated at the global and local spatial scales, which requires accurate consideration of the return flow due to the tide back-and-forth movements.

4.2.1. *e*-folding flushing time

The water renewal time is based on an eulerian reference system. It estimates the dilution time scale of a passive tracer released within a control domain. It indicates the time spent for exchange water masses with new water coming from both the sea and the rivers discharging into the basin. In our case, the control domain is made of the whole inside volume of the bay plus the external part linked to its tidal prism computed in mean tide conditions (see dash blue line in Fig. 8). The return flow through the Goulet due to the semi-diurnal tide must be accounted for in the estimation of the renewal time scales. As recommended by Viero and Defina (2016), the simulated domain must be larger than the control volume. This can be done by using the two-way nesting and update skills of AGRIF. The initial concentration of a passive tracer is set to 1 inside the control domain (in the fine grid) and 0 elsewhere. After the release, only waters coming from the ocean (outside the Iroise sea) and the river's runoffs are fixed with a tracer concentration equal to 0. The outflow concentrations are then lost when crossing the model grid (mother grid in two-way nesting). The back-and-forth flow through the control volume border is taken into account. For each grid cell, the flushing lag t_0 represent the time decrease for the concentration to reach 95%. It enables to understand the evolution of water coming from outside or river within the control volume. Then the local flushing time θ is estimated in each grid cell as the time decrease in concentration from 95% up to $1/e$ of initial concentration using an exponential regression $C(t - t_0) = e^{-(t-t_0)/\theta}$ (Jouon et al., 2006; Grifoll et al., 2013; Plus et al., 2009). The removing of flushing lag enables a better regression for areas far away from the volume's boundaries especially for geographic complex area. A global flushing indicator is also estimated for the whole control volume using the same method without the lag dependency. To get rid of the initial tide conditions (Plus et al., 2009), 13 tracers are separately released every hour for an even coverage of the tidal cycle. The final indicator is an average of the 13 solutions.

4.2.2. Case scenario

Various numerical experiments have been performed to catch variable conditions and estimate an exhaustive renewal indicator. Each simulation has been carried out according to the same protocol with a hydrodynamic spin-up run performed over one month before the release of passive tracers. To obtain various tidal regimes and hydrologic runoffs, the study focuses on four scenarios with respect to the tidal range combined with two different runoffs: Releases have been done at the beginning of spring tides and neap tides, in winter and summer seasons during a flood and a low-flow events. All of these simulations have been performed with realistic atmospheric forcings. A detailed description of the scenarios is given in Table 4.

Table 4: Environmental condition for each computation periods mean over the first 30 days of simulation

Scenario	Initial dates of modelling	Cumulated Aulne river flow (10^6 m³)	Wind velocity ± SD (m.s⁻¹) and direction (°)
Low water – Neap tide	Jan 29th 2016	380.3	8.43 ± 4.0 (257°)
Low water – Spring tide	Feb 6th 2016	337.7	8.29 ± 4.2 (274°)

16

Flood – Neap tide	Aug 8th 2015	13.7	4.69 ± 2.6 (281°)
Flood – Spring tide	Jul 29th 2015	10.5	4.97 ± 2.7 (242°)

4.3. Flushing times of the Bay of Brest

The question addressed here is to identify the role played by the tidal forcing and water runoffs on the renewal capacity of the

470   bay. Although wind direction and intensity are highly variables at mid-latitude, it has been decided not to focus on meteorological effects because it is difficult to find 15-days wind sequences that characterize the local atmospheric forcings. In addition, the bay is a highly energetic coastal area with strong diffusive and dispersive characteristics as its regime is macro-tidal. Then, the focus is on the two dominant runoff regimes (flood water *vs* low water) combined with the initial phase of the tide (spring *vs* neap tides).

475   The renewal indicator has been estimated with both nesting methods for the four scenarios. The flushing times of the whole volume are given in Table 5. For each simulation, this timescale features the lowest value for a release at low tide with a maximum variation of 1.4 day. As expected, low water runoffs imply larger renewal time compared to flood situation. However, the initial tidal phase is the main factor of change between the scenarios with a more intensive mixing in spring tides. There is a positive offset (roughly 10%) when the AGRIF two-way nesting is used for the estimation of this indicator.

480   This is due to the return flow inside the bay during each tidal cycle that is under-estimated in the one-way model as its boundaries act as a sink for the tracer.

Table 5: Global *e*-flushing times and standard deviation in days for the whole control volume for both modelized configurations. The deviation is estimated over the 13 time released simulations for each scenario.

	Global *e*-flushing time in days	
Scenario	**one-way**	**two-way**
Low water – Neap tide	11.29 ± 0.42	12.23 ± 0.64
Low water – Spring tide	7.68 ± 0.39	8.34 ± 0.48
Flood – Neap tide	10.22 ± 0.41	10.84 ± 0.53
Flood – Spring tide	6.95 ± 0.35	7.85 ± 0.53

485   The local *e*-flushing times estimated with the two-way nesting configuration in low-water conditions are displayed for initial spring tide (Fig. 9a) and neap tide (Fig. 9b). In the same way, the renewal indicator is shown for flood conditions for initial spring tide (Fig. 9c) and neap tide (Fig. 9d). The coefficient increases with the geographic position relative to the border of the control volume. In opposition to the computation of global indicator, here the impact of runoff is clearly visible in the

renewal capacity of the bay. In low water condition, the south-eastern part of the bay is clearly isolated from the rest. The

490 range of local *e*-flushing time reaches more than 25 days in shallow coves for a release at neap tide. The impact of tide is the next level in order of importance with, not surprisingly, stronger renewal during spring tide than neap tide. In each scenario, the central energetic eddy stands out because it is the rallying point of continental waters.

Some particular structures appear at the western part of the control volume. This is due to a weak exponential regression where the residuals between exponential decay and simulation result are below 0.5. This part of the domain was only there to account

495 for the tidal prism extent. A similar issue occurs next to the river mouths. Both problems are due to the initial time release over the first tide cycle. This is easily understandable for areas next to the volume limits in the ocean. For river mouth, de Brauwere et al. (2011) pointed out than initial time release in estuaries could lead to extreme different values, as it is here between a release at high tide and low tide. However, the fact of considering the initial flushing lag (ranging from few hours up to 7 days) in each mesh strengthened considerably the *e*-folding regression approach.

500 With one-way nesting, the relative differences of *e*-folding flushing time for each mesh are shown in Fig. 10 in the same order than Fig. 9. First, spring (Fig. 10a) and neap (Fig. 10b) tides in low water condition and second spring (Fig. 10c) and neap (Fig. 10d) tides in flood condition. The one-way nesting overestimates in each cases the renewal capacity of the bay by predicting lower local *e*-folding flushing time nearly everywhere. In the inner part of the bay, the local differences are always negative and reach around 20% in flood conditions. Under low water condition, although there are no changes for the energetic

505 water mass in the central part, the discrepancies appear in the eastern part of the bay and in shallow areas. Here again for each scenario, the structures at the limits of the control volume are not clear for any scenario and present sharp extents with alternation of under and over-estimations. To testify to the veracity of the over-estimation of one-way nesting, a similar approach was used with a far smaller control volume located only inside the bay. As the simulated domain is larger than the control volume, results were the same between nesting methods.

510 The improvement of the AGRIF two-way nesting consists both in the refining of coastal areas where water renewal is the most critical and in properly tracking the tidal prism enclosed in the global, advected and time-dispersed control volume. The known methods used to estimate such parameters are generally constraint to the definition of a global control of volume. This volume is tightly related to the geographic context and the environmental study objectives. The management of the open boundaries for the fine grid is a key element to address properly this issue. In the case of a standalone grid, when the flow is entering the

515 domain at the open boundaries, the user can usually either chose to apply or nudge towards a constant value (zero or whatever value), a time series inferred from large scale solution (if available) or a zero-gradient condition. In any case, the chosen solution is highly non conservative, resulting in discrepancies for the final indicators. The two-way nesting enables the correct estimation of flushing parameters in the Bay of Brest, which requires accurate tracking of the tidal prism encompassed in the control volume across time. Here, a significant part of water is tidally flushed from the bay and spread to the Iroise sea with

520 diffusion processes. The AGRIF capability improves the management of the fate of a tracer outside the bay at the coarser horizontal resolution (and at fairly reasonable computational cost) and enforces accurate incoming concentration along the

open boundaries on the child grid. This conservative approach is required for an accurate estimation of the indicators. It is also relevant for applications with sedimental, biological or chemical dynamics models that can be coupled.

5. Discussion

525   The present study demonstrates the capabilities of MARS3D/AGRIF two-way nesting. The very first objective of grid refinement is either to tackle a local stationary problem or to follow a single dynamical structure along to its displacements (Blayo and Debreu, 1999). The zoom is there to reach a relevant resolution (*e.g.,* commensurable with the Rossby internal radius or with the geometry of a given structure or set of structures such as islands, capes or peninsulas) raising the major question which lies in the downscaling of global and coarse information to the resolution of the targeted area at least at the

530   open boundaries of the considered domain.

Despite the regular improvement in the computational power available for high-performance scientific computing, the computational cost and the storage of huge datasets remain major issues for long-term numerical oceanic simulations, due to various reasons such as green computing considerations. We hereafter review the different key advantages provided by the AGRIF library as used in a semi-implicit free surface ocean model set on a structured grid.

535   Regarding parametrization, the AGRIF library allows the specification of a distinctive parametrisation for each grid of the hierarchy (meteorological forcings, runoffs, vertical turbulence scheme, surface and bottom friction coefficients…). In addition to the different physical parametrizations well suited to local process, a local time refinement is performed to fit to the local dynamics: each grid of the hierarchy can have its own sub-temporal integration as used in the regional configuration (ratio of 3 to 5). The more the dynamics is intense the more the time refinement factor is increased. Whereas for areas where the stability

540   condition is more binding, the time refinement factor can be diminished.

The AGRIF flexibility also lies in the way child grid in a given hierarchy can be either added or easily removed: the addition of a grid requires the coupling of this additional child grid bathymetry with the bathymetries of the other grids. An offline bathymetric update algorithm, available with MARS3D code, modifies both mother and child bathymetries in order to fit fluxes (from one grid to another) along child borders. Once the bathymetry consistency is performed along the boundaries

545   between the mother and child grids, the user can launch the runs without additional tasks. The initial conditions for the new zoom are estimated online at the first timestep by the AGRIF library. This capability has been used to study more precisely the deep convection in the northwestern mediterranean sea (Garreau and Garnier, 2015) or to better identify shear stress over future renewable marine energy structures (Maisondieu, Pers. comm). In situations where the user needs to remove a specific child grid, the mother grid's bathymetry has just to be recomputed before launching the model.

550   The usual offline nesting procedure requires writing and storage of 3D forcing files from which the open boundary and initial conditions for the child grid are supplied. In order to avoid aliasing or spurious incompatibilities between barotropic and baroclinic modes, high frequency output to hard disk is required; in the most penalizing cases, for example where tidal dynamics are dominant, it involves a huge amount of I/O, which raises other kinds of issues such as how to write massive data

in a massive parallel context. Despite the many improvements to deal with this question, like deporting the I/O on dedicated

555 CPUs as it is the case in the XIOS library (Yepes-Arbós et al., 2022), they cannot escape the cost of long-term storage of massive data. This is even more obvious in case of several nested grids in the same mother grid (such as the Bay of Biscay configuration) which would extend the pre-processing step to create child boundaries and require more flexibility than AGRIF provides. The on-the-fly grid nesting procedure (encompassing initial and open boundaries management) included in the two-way nesting circumvents these tedious steps by performing them online at each time step, and for the different grids of the

560 hierarchy.

Another point concerns the vertical coordinate framework which is here a sigma framework. The vertical interpolation towards a sigma framework requires most of the time the projection onto a geopotential framework in order to perform the split horizontal-vertical interpolation: the horizontal interpolation consists of the rescaling from the coarse to the fine horizontal grid whereas, the vertical interpolation mainly consists in a resampling of the vertical levels without any changes in the overall

565 resolution (or the use of a kriging method). The side effects of the split interpolation on temperature and salinity fields can lead to gravity instabilities in case of large bathymetric inconsistencies between the coarse and child grids. Therefore, the user hast to carefully define interpolation parameters (such as those defining the intermediate geopotential framework onto which the vertical interpolation is performed) and check the consistency of the gravity gradient. As MARS3D/AGRIF two-way nesting requires a perfect fitting of the vertical discretization of all grids of the hierarchy and bathymetries coherence, these

570 constraints prevent the gravity issues. This kind of very well-known problem may also be avoided in offline embedment procedure by taking the same care in defining the grid and the bathymetry computations. Nevertheless, this vertical coherence may lead to over-resolved vertical grids. Then reducing the number of vertical levels from mother to child grid is not possible to save precious computing power when resolving vertical dynamic process in well-mixed areas.

The traditional one-way nesting remains a lighter solution than AGRIF two-way, especially in case one has to perform repeated

575 experiments for tuning purpose with different parametrizations or different environmental hypothesis (Cadier et al., 2017; Petton et al., 2020; Gangnery et al., 2019). As open boundary files can be re-used at no cost, this method still is a good approach to improve important numerical developments in coastal model. However, the two-way update process is needed when final objective is to assure a conservative approach (biological tracer, connectivity study…) over large geographic area at minimum cost. It is not a unique solution; other kinds of spatial discretization such as unstructured, curvilinear or polar-style coordinates

580 meet the same numerical constraints. The two-way nesting proposed here keeps it simple for the end-user.

As shown in Sect. 3.2, the online interpolation from mother to child grid and the update process preserve the propagation of tidal elevations and currents with an equivalent level of accuracy than the one achieved with the tidal forcing prescribed at open boundary conditions of a single typical coastal grid (some tens of kilometres of extension, in 10 to 100 m depth, at some hundreds of meters of resolution). For this type of standalone grid, validated harmonic atlas at high horizontal resolution (*i.e.*

585 from 750 m to 250 m, Pineau-Guillou, 2013) may be available: enabling to represent accurately the tidal elevations and currents within the encompassed area. According to the slow varying characteristics of the tidal components this downscaling approach can be thought to be performed only once by generating a reference tidal atlas. In the two-way nesting approach depicted here,

20

the tidal propagation computed at the coarse grid level is fed with a global reference tidal solution, either TPXO (Egbert and Erofeeva, 2002) or FES (Lyard et al., 2021). For the regional configuration exposed previously, the tide coming from the mother grid with the two-way nesting has been only computed with the global FES model. The observed differences between the one-way offline and the two-way nesting methods are less than a few centimetres which are not really significant in coastal areas. It relies mainly on the continuity of the mass fluxes at the interface between the child and the coarse grids. This functionality is preserved thanks to the AGRIF library implementation and allows MARS3D to represent tides at regional scales and medium resolution (Lazure et al., 2009; Muller et al., 2014).

This software also has the capability to perform the opposite, that is to say grid coarsening. It is a relevant capability for on-line physical-biogeochemical coupling which was used for example by Lévy et al. (2012) in an offline mode. Capturing relevant scales of the oceanic flows may require higher spatial resolution than the main feature of biogeochemical fields. In such a case, it is essential to solve the submesoscale features that enhance the vertical exchange and consequently refuel the surface with nutrients. The required resolution, of the order of a few hundred meters, is unaffordable for state-of-the-art biogeochemical models that use and advect tens of tracers fields (Heinze and Gehlen, 2013). The AGRIF coarsening capability allows this differential resolution (physics at high-resolution, biogeochemistry at lower resolution) by building on-line non-divergent transport fields from the high-resolution grid on the coarse resolution grid. In that way, the "grand-mother" grid may completely overlap the mother grid.

In contrast, another perspective for the AGRIF library is to generalize the refinement approach towards what is called a multi-resolution approach (Debreu et al., 2016): adding not only a few grids but tens to hundreds of grids with numerous hierarchical level in order to pave the space systematically according to refinement criteria (distance to the coast, bathymetric threshold…). This alternative involves the creation of a thin pavement next to the coast which is encompassed in a coarser pavement and so on. The integration of numerous grids of various size with various overlapping is not straightforward in massive parallel computational framework. It raises many questions of load balance, processors dispatching, communication blocking, etc… Another concern is the data format structure used for the I/O: The duplication of data over same areas at different levels increases disk demand. In order to boost writing and to perform postprocessing diagnostic and visualisation, further improvements are required to elaborate a special structure with the minimal overlap data.

6. Conclusions

Algorithms for the implementation of two-way structured mesh refinement in a semi-implicit free surface ocean model are described in this paper. For coastal applications, the correct treatment of wetting and drying requires a careful design of the grid interactions. Applications of such a mesh refinement technique allow reaching very high-resolution all along the French coast of the Bay of Biscay featured by a macro-tidal regime. The present analyses demonstrate the positive impact of the two-way refinement against simple one-way refinement. In addition to the applications presented here, these mesh refinement capabilities have now been validated on a series of realistic configurations.

620   The computational aspects of grid refinement are managed by the AGRIF software. In the context of sustainable green computing, this nesting technique saves tedious file processing and interpolation steps. It is well suited for large configurations with several zoom models, for long-term hindcast or operational forecast simulations to monitor the marine environment. The AGRIF implementation in the MARS3D model provides the opportunity to the users to easily activate or deactivate a given child grid. Adding one additional zoom level is a quick process which actually relies more on the accuracy of the available

625   bathymetric data than on technical issues. In coastal areas, the two-way nesting solution enables the correct estimation of environmental indicators calculated for highly different hydrologic and tidal forcing in order to characterize the general mixing of the bay. It allows the fine simulation of biological processes that require mass conservation at large scales with different horizontal resolution.

Appendices

630   **A. Data used for validation**

The tidal validation is based on four stations from the French tidal gauge network RONIM maintained by the SHOM. Moreover, three datasets are available in the framework of the national program COAST-HF (Coastal Ocean Observing System-High Frequency, www.coast-hf.fr) which gathers fourteen automated moored buoys. The COAST-HF ASTAN buoy (48.749°N; 3.961°W) is a cardinal buoy of opportunity located 3.1 km offshore from Roscoff, east of the Batz Island. It records

635   data every 30 minutes at 5-meter depth since 2008 (Gac et al., 2020), over a mean bathymetry of 45 m. The COAST-HF MAREL-Iroise buoy (48.357°N, 4.582°W) is located at the entrance of the bay of Brest and records data every 20 minutes at 2-meter depth since 2000 (Rimmelin-Maury et al., 2020). Inside the bay of Brest next to the Mignonne river mouth, the COAST-HF SMART-Daoulas buoy (48.317°N, 4.331°W) is monitoring parameters at 50 cm over the seabed at 15-mins frequency since 2016 (Petton et al., 2021b). Next to this last point, the Ifremer observatory network ECOSCOPA has a study

640   site called Pointe du Château (48.335°N, 4.319°W) on an oyster farm in the intertidal zone. Temperature and salinity data are available at a 15-mins frequency since 2008 (Petton et al., 2021a). We also had access to the sea surface temperature data from the Datawell buoy of les Pierres Noires which is part of the swell monitoring network CANDHIS (CEREMA) and located in the middle of the Iroise Sea (48.29°N, 4.97°W). These monitoring stations are presented in Fig. 5 and Fig. 8.

Besides, satellite data are used for sea surface temperature validation at two different horizontal scales: The first one is based

645   on SST fields extracted from the global Advanced Very High Resolution Radiometer (AVHRR) Pathfinder V5 daily dataset. The ODYSSEA chain has been modified by Saulquin and Gohin, (2010) to use optimal interpolation for the reconstruction of gap-free and using the previous analysis as a first guess. The product is gridded at a 0.02° spatial resolution and freely available at https://resources.marine.copernicus.eu (Autret and Piollé, 2018). The second one is based on the Thermal InfraRed Sensor (TIRS) from the Landsat 8 satellite. As it orbits the Earth in a sun-synchronous, near-polar orbit inclined at 98.2 degrees, one

650   gets a track over our area of interest every 8 days. Consequently, it is hard to extract snapshots without too much clouds. Recently the United States Geological Survey (USGS) has started to distribute Landsat Collection 2 Level 2 (values are given

after atmospheric corrections) with a calibrated land surface temperature field. The development of a water temperature algorithm is not the aim of this paper and represents a challenge by itself (Vanhellemont, 2020). However, the use of such high-resolution product (30m gridded) is very useful to detect fine structures. In that respect, the ODYSSEA product is complementary to the Landsat 8 scene and a reference on a coarser grid. To discriminate water temperature from cloud or land value, the quality index given for each pixel for this collection is used.

Code availability

Last version of MARS3D is freely available on request at https://wwz.ifremer.fr/mars3d/. The AGRIF library is freely available at under CECILL license (http://www.cecill.info). Both codes are written in Fortran-90/95 and figures are displayed from python scripts or with QGIS software for both configuration presentations. All the model code, bathymetric grid files, namelist configuration files for both regional and coastal applications and python scripts used in this paper are available at https://doi.org/10.5281/zenodo.6672562.

Data availability

All data used in this paper are freely available from their DOI repository.

Author contribution

LD has developed the AGRIF Library. LD, VG and FD have integrated the AGRIF library in the MARS3D model. MC and SP have setup the model configurations, adapted the AGRIF integration to coastal environment and provided figures for the paper. All authors have contributed to the concepts and the writing of the paper.

Competing interest

The contact author has declared that neither he nor their co-authors have any competing interests.

Financial support

References

Auffret, G.-A.: Dynamique sédimentaire de la marge continentale celtique - Evolution Cénozoïque - Spécificité du Pleistocène supérieur et de l'Holocène, Université de Bordeaux I, 1983.

Autret, E. and Piollé, J.-F.: European North West Shelf/Iberia Biscay Irish Seas - High Resolution ODYSSEA L4 Sea Surface
680 Temperature Analysis, https://doi.org/https://doi.org/10.48670/moi-00152, 2018.

Bacher, C., Filgueira, R., and Guyondet, T.: Probabilistic approach of water residence time and connectivity using Markov chains with application to tidal embayments, J. Mar. Syst., 153, 25–41, https://doi.org/10.1016/j.jmarsys.2015.09.002, 2016.

Bendtsen, J., Gustafsson, K. E., Söderkvist, J., and Hansen, J. L. S.: Ventilation of bottom water in the North Sea–Baltic Sea transition zone, J. Mar. Syst., 75, 138–149, https://doi.org/10.1016/J.JMARSYS.2008.08.006, 2009.

685 Berger, M. J. and Oliger, J.: Adaptive mesh refinement for hyperbolic partial differential equations, J. Comput. Phys., 53, 484–512, https://doi.org/https://doi.org/10.1016/0021-9991(84)90073-1, 1984.

Bezaud, M. and Pineau-Guillou, L.: Qualification des modèles hydrodynamiques 3D des côtes de la Manche et de l'Atlantique, 158 pp., 2015.

Biastoch, A., Böning, C. W., Schwarzkopf, F. U., and Lutjeharms, J. R. E.: Increase in Agulhas leakage due to poleward shift
690 of Southern Hemisphere westerlies, Nature, 462, 495–498, https://doi.org/10.1038/nature08519, 2009.

Biastoch, A., Sein, D., Durgadoo, J. V, Wang, Q., and Danilov, S.: Simulating the Agulhas system in global ocean models – nesting vs. multi-resolution unstructured meshes, Ocean Model., 121, 117–131, https://doi.org/10.1016/j.ocemod.2017.12.002, 2018.

Blayo, E. and Debreu, L.: Adaptive Mesh Refinement for Finite-Difference Ocean Models: First Experiments, J. Phys.
695 Oceanogr., 29, 1239–1250, https://doi.org/10.1175/1520-0485(1999)029<1239:AMRFFD>2.0.CO;2, 1999.

Bolin, B. and Rodhe, H.: A note on the concepts of age distribution and transit time in natural reservoirs, Tellus, 25, 58–62, https://doi.org/10.1111/j.2153-3490.1973.tb01594.x, 1973.

de Brauwere, A., de Brye, B., Blaise, S., and Deleersnijder, E.: Residence time, exposure time and connectivity in the Scheldt Estuary, J. Mar. Syst., 84, 85–95, https://doi.org/10.1016/j.jmarsys.2010.10.001, 2011.

700 Cadier, M., Gorgues, T., Sourisseau, M., Edwards, C. A., Aumont, O., Marié, L., and Memery, L.: Assessing spatial and temporal variability of phytoplankton communities' composition in the Iroise Sea ecosystem (Brittany, France): A 3D modeling approach. Part 1: Biophysical control over plankton functional types succession and distribution, J. Mar. Syst., 165, 47–68, https://doi.org/https://doi.org/10.1016/j.jmarsys.2016.09.009, 2017.

Inter annual hydrodynamic hindcast with MARS3D-AGRIF model - Bay of biscay and Manche Areas:

705 Capet, X.: Contributions to the understanding of meso/submesoscale turbulence and their impact on the ocean functioning, UPMC - Université Paris 6 Pierre et Marie Curie, 2015.

Debreu, L. and Blayo, E.: Two-way embedding algorithms: a review, Ocean Dyn., 58, 415–428, https://doi.org/10.1007/s10236-008-0150-9, 2008.

Debreu, L., Vouland, C., and Blayo, E.: AGRIF: Adaptive grid refinement in Fortran, Comput. Geosci., 34, 8–13, https://doi.org/10.1016/j.cageo.2007.01.009, 2008.

Debreu, L., Marchesiello, P., Penven, P., and Cambon, G.: Two-way nesting in split-explicit ocean models: Algorithms, implementation and validation, Ocean Model., 49–50, 1–21, https://doi.org/https://doi.org/10.1016/j.ocemod.2012.03.003, 2012.

Debreu, L., Auclair, F., Benshila, R., Capet, X., Dumas, F., Julien, S., and Marchesiello, P.: Multiresolution in CROCO (Coastal and Regional Ocean Community model), in: EGU General Assembly Conference Abstracts, EPSC2016-15272, 2016.

Delandmeter, P., Lambrechts, J., Legat, V., Vallaeys, V., Naithani, J., Thiery, W., Remacle, J.-F., and Deleersnijder, E.: A fully consistent and conservative vertically adaptive coordinate system for SLIM 3D v0.4 with an application to the thermocline oscillations of Lake Tanganyika, Geosci. Model Dev., 11, 1161–1179, https://doi.org/10.5194/gmd-11-1161-2018, 2018.

Deleersnijder, E., Campin, J.-M. M., and Delhez, E. J. M.: The concept of age in marine modelling I. Theory and preliminary model results, J. Mar. Syst., 28, 229–267, https://doi.org/10.1016/S0924-7963(01)00026-4, 2001.

Delhez, E. J. M.: Transient residence and exposure times, Ocean Sci., 2, 1–9, https://doi.org/10.5194/os-2-1-2006, 2006.

Delhez, É. J. M., Heemink, A. W., and Deleersnijder, É.: Residence time in a semi-enclosed domain from the solution of an adjoint problem, Estuar. Coast. Shelf Sci., 61, 691–702, https://doi.org/10.1016/j.ecss.2004.07.013, 2004.

Diaz, M., Grasso, F., Le Hir, P., Sottolichio, A., Caillaud, M., and Thouvenin, B.: Modeling Mud and Sand Transfers Between a Macrotidal Estuary and the Continental Shelf: Influence of the Sediment Transport Parameterization, J. Geophys. Res. Ocean., 125, e2019JC015643, https://doi.org/https://doi.org/10.1029/2019JC015643, 2020.

Dufois, F., Verney, R., Le Hir, P., Dumas, F., and Charmasson, S.: Impact of winter storms on sediment erosion in the Rhone River prodelta and fate of sediment in the Gulf of Lions (North Western Mediterranean Sea), Cont. Shelf Res., 72, 57–72, https://doi.org/https://doi.org/10.1016/j.csr.2013.11.004, 2014.

Egbert, G. D. and Erofeeva, S. Y.: Efficient Inverse Modeling of Barotropic Ocean Tides, J. Atmos. Ocean. Technol., 19, 183–204, https://doi.org/10.1175/1520-0426(2002)019<0183:EIMOBO>2.0.CO;2, 2002.

Fiandrino, A., Ouisse, V., Dumas, F., Lagarde, F., Pete, R., Malet, N., Le Noc, S., and de Wit, R.: Spatial patterns in coastal lagoons related to the hydrodynamics of seawater intrusion, Mar. Pollut. Bull., 119, 132–144, https://doi.org/10.1016/j.marpolbul.2017.03.006, 2017.

Frère, L., Paul-Pont, I., Rinnert, E., Petton, S., Jaffré, J., Bihannic, I., Soudant, P., Lambert, C., and Huvet, A.: Influence of environmental and anthropogenic factors on the composition, concentration and spatial distribution of microplastics: A case study of the Bay of Brest (Brittany, France), Environ. Pollut., 225, 211–222, https://doi.org/10.1016/j.envpol.2017.03.023, 2017.

Gac, J.-P., Marrec, P., Cariou, T., Guillerm, C., Macé, É., Vernet, M., and Bozec, Y.: Cardinal Buoys: An Opportunity for the Study of Air-Sea CO2 Fluxes in Coastal Ecosystems, Front. Mar. Sci., 7, https://doi.org/10.3389/fmars.2020.00712, 2020.

Gangnery, A., Normand, J., Duval, C., Cugier, P., Grangeré, K., Petton, B., Petton, S., Orvain, F., and Pernet, F.: Connectivities

with Shellfish Farms and Channel Rivers are Associated with Mortality Risk in Oysters, Aquac. Environ. Interact., 11, 493–506, https://doi.org/10.3354/aei00327, 2019.

745 Garreau, P. and Garnier, V.: Physical processes acting in a numerical oceanic model during the convection period of SOP2, in: 9th HyMeX workshop, 21-25 September 2015, Mykonos, Greece, Oral, 2015.

Grasso, F., Verney, R., Le Hir, P., Thouvenin, B., Schulz, E., Kervella, Y., Khojasteh Pour Fard, I., Lemoine, J.-P., Dumas, F., and Garnier, V.: Suspended Sediment Dynamics in the Macrotidal Seine Estuary (France): 1. Numerical Modeling of Turbidity Maximum Dynamics, J. Geophys. Res. Ocean., 123, 558–577,
750 https://doi.org/https://doi.org/10.1002/2017JC013185, 2018.

Grifoll, M., Del Campo, A., Espino, M., Mader, J., González, M., and Borja, Á.: Water renewal and risk assessment of water pollution in semi-enclosed domains: Application to Bilbao Harbour (Bay of Biscay), J. Mar. Syst., 109–110, S241–S251, https://doi.org/10.1016/j.jmarsys.2011.07.010, 2013.

Heinze, C. and Gehlen, M.: Modeling Ocean Biogeochemical Processes and the Resulting Tracer Distributions, in: Ocean
755 Circulation and Climate, vol. 103, edited by: Siedler, G., Griffies, S. M., Gould, J., and Church, J. A. B. T.-I. G., Academic Press, 667–694, https://doi.org/10.1016/B978-0-12-391851-2.00026-X, 2013.

Huret, M., Sourisseau, M., Petitgas, P., Struski, C., Léger, F., and Lazure, P.: A multi-decadal hindcast of a physical-biogeochemical model and derived oceanographic indices in the Bay of Biscay, J. Mar. Syst., 109–110, https://doi.org/10.1016/j.jmarsys.2012.02.009, 2013.

760 Janin, J. M., Lepeintre, F., Pechon, P., and de France. Direction des études et recherches. Service Applications de l'electricité et environnement, E.: Telemac-3d : a Finite Element Code to Solve 3D Free Surface Flow Problems:, EDF-DER, 1993.

Jiang, C., Liu, Y., Long, Y., and Wu, C.: Estimation of Residence Time and Transport Trajectory in Tieshangang Bay, China, Water, 9, 321, https://doi.org/10.3390/w9050321, 2017.

Jordi, A., Ferrer, M. I., Vizoso, G., Orfila, A., Basterretxea, G., Casas, B., Álvarez, A., Roig, D., Garau, B., Martínez, M.,
765 Fernández, V., Fornés, A., Ruiz, M., Fornós, J. J., Balaguer, P., Duarte, C. M., Rodríguez, I., Alvarez, E., Onken, R., Orfila, P., and Tintoré, J.: Scientific management of Mediterranean coastal zone: A hybrid ocean forecasting system for oil spill and search and rescue operations, Mar. Pollut. Bull., 53, 361–368, https://doi.org/10.1016/j.marpolbul.2005.10.008, 2006.

Jouon, A., Douillet, P., Ouillon, S., and Frauníe, P.: Calculations of hydrodynamic time parameters in a semi-opened coastal zone using a 3D hydrodynamic model, Cont. Shelf Res., 26, 1395–1415, https://doi.org/10.1016/j.csr.2005.11.014, 2006.

770 Kininmonth, S. J., De'ath, G., and Possingham, H. P.: Graph theoretic topology of the Great but small Barrier Reef world, Theor. Ecol., 3, 75–88, https://doi.org/10.1007/s12080-009-0055-3, 2010.

Lazure, P. and Dumas, F.: An external–internal mode coupling for a 3D hydrodynamical model for applications at regional scale (MARS), Adv. Water Resour., 31, 233–250, https://doi.org/10.1016/J.ADVWATRES.2007.06.010, 2008.

Lazure, P., Garnier, V., Dumas, F., Herry, C., and Chifflet, M.: Development of a hydrodynamic model of the Bay of Biscay.
775 Validation of hydrology, Cont. Shelf Res., 29, 985–997, https://doi.org/10.1016/j.csr.2008.12.017, 2009.

Leendertse, J. J. and Gritton, E. C.: A water quality simulation model for well mixed estuaries and coastal seas: Vol. II,

Computation Procedures, 1971.

Lévy, M., Resplandy, L., Klein, P., Capet, X., Iovino, D., and Ethé, C.: Grid degradation of submesoscale resolving ocean models: Benefits for offline passive tracer transport, Ocean Model., 48, 1–9, https://doi.org/https://doi.org/10.1016/j.ocemod.2012.02.004, 2012.

Li, J. G.: Filling oceans on a spherical multiple-cell grid, Ocean Model., 157, 101729, https://doi.org/10.1016/j.ocemod.2020.101729, 2021.

Lucas, L. V. and Deleersnijder, E.: Timescale Methods for Simplifying, Understanding and Modeling Biophysical and Water Quality Processes in Coastal Aquatic Ecosystems: A Review, Water, 12, 2717, https://doi.org/10.3390/w12102717, 2020.

Lyard, F. H., Allain, D. J., Cancet, M., Carrère, L., and Picot, N.: FES2014 global ocean tide atlas: design and performance, Ocean Sci., 17, 615–649, https://doi.org/10.5194/os-17-615-2021, 2021.

Marchesiello, P., Capet, X., Menkes, C., and Kennan, S. C.: Submesoscale dynamics in tropical instability waves, Ocean Model., 39, 31–46, https://doi.org/10.1016/j.ocemod.2011.04.011, 2011.

Marsaleix, P., Auclair, F., and Estournel, C.: Considerations on Open Boundary Conditions for Regional and Coastal Ocean Models, J. Atmos. Ocean. Technol., 23, 1604–1613, https://doi.org/10.1175/JTECH1930.1, 2006.

Meier, H. E. M.: Modeling the age of Baltic Seawater masses: Quantification and steady state sensitivity experiments, J. Geophys. Res. Ocean., 110, https://doi.org/10.1029/2004JC002607, 2005.

Monsen, N. E., Cloern, J. E., Lucas, L. V, and Monismith, S. G.: A comment on the use of flushing time, residence time, and age as transport time scales, Limnol. Oceanogr., 47, 1545–1553, https://doi.org/10.4319/lo.2002.47.5.1545, 2002.

Muller, H., Blanke, B., Dumas, F., Lekien, F., and Mariette, V.: Estimating the Lagrangian residual circulation in the Iroise Sea, J. Mar. Syst., 78, S17–S36, https://doi.org/https://doi.org/10.1016/j.jmarsys.2009.01.008, 2009.

Muller, H., Pineau-Guillou, L., Idier, D., and Ardhuin, F.: Atmospheric storm surge modeling methodology along the French (Atlantic and English Channel) coast, Ocean Dyn., 64, 1671–1692, https://doi.org/10.1007/s10236-014-0771-0, 2014.

Naranjo, C., Garcia-Lafuente, J., Sannino, G., and Sanchez-Garrido, J. C.: How much do tides affect the circulation of the Mediterranean Sea? From local processes in the Strait of Gibraltar to basin-scale effects, Prog. Oceanogr., 127, 108–116, https://doi.org/https://doi.org/10.1016/j.pocean.2014.06.005, 2014.

Neal, V. T.: PREDICTED FLUSHING TIMES AND POLLUTION DISTRIBUTION IN THE COLUMBIA RIVER ESTUARY, Coast. Eng. Proc., 1, 81, https://doi.org/10.9753/icce.v10.81, 1966.

Le Pape, O. and Menesguen, A.: Hydrodynamic prevention of eutrophication in the Bay of Brest (France), a modelling approach, J. Mar. Syst., 12, 171–186, https://doi.org/10.1016/S0924-7963(96)00096-6, 1997.

Penven, P., Debreu, L., Marchesiello, P., and McWilliams, J. C.: Evaluation and application of the ROMS 1-way embedding procedure to the central california upwelling system, Ocean Model., 12, 157–187, https://doi.org/https://doi.org/10.1016/j.ocemod.2005.05.002, 2006.

Petton, S. and Dumas, F.: MARS3D / AGRIF model configuration for the Bay of Brest, https://doi.org/10.17882/86400, 18 February 2022.

Petton, S., Pouvreau, S., and Dumas, F.: Intensive use of Lagrangian trajectories to quantify coastal area dispersion, https://doi.org/10.1007/s10236-019-01343-6, 2020.

Petton, S., Le Roy, V., Bellec, G., Queau, I., Le Souchu, P., and Pouvreau, S.: Marine environmental station database of Daoulas bay, https://doi.org/10.17882/42493, 2021a.

815 Petton, S., Le Roy, V., and Pouvreau, S.: SMART Daoulas data from coriolis Data Centre in the Bay of Brest, https://doi.org/10.17882/86020, January 2021b.

Pineau-Guillou, L.: PREVIMER. Validation des atlas de composantes harmoniques de hauteurs et courants de marée, Ifremer, Ifremer, France, 2013.

Piton, V., Herrmann, M., Lyard, F., Marsaleix, P., Duhaut, T., Allain, D., and Ouillon, S.: Sensitivity study on the main tidal
820 constituents of the Gulf of Tonkin by using the frequency-domain tidal solver in T-UGOm, Geosci. Model Dev., 13, 1583–1607, https://doi.org/10.5194/gmd-13-1583-2020, 2020.

Plus, M., Dumas, F., Stanisière, J. Y., and Maurer, D.: Hydrodynamic characterization of the Arcachon Bay, using model-derived descriptors, Cont. Shelf Res., 29, 1008–1013, https://doi.org/10.1016/j.csr.2008.12.016, 2009.

Rétif, F., Bouchette, F., Marsaleix, P., Liou, J.-Y., Meulé, S., Michaud, H., Lin, L.-C., Hwang, K.-S., Bujan, N., Hwung, H.-
825 H., and Team, S.: REALISTIC SIMULATION OF INSTANTANEOUS NEARSHORE WATER LEVELS DURING TYPHOONS, Coast. Eng. Proc., 1, waves.17, https://doi.org/10.9753/icce.v34.waves.17, 2014.

Rimmelin-Maury, P., Charria, G., Repecaud, M., Quemener, L., Beaumont, L., Guillot, A., Gautier, L., Prigent, S., Le Becque, T., Bihannic, I., Bonnat, A., Le Roux, J.-F., Grossteffan, E., Devesa, J., and Bozec, Y.: Iroise buoy data from Coriolis data center as core parameter support for Brest Bay and Iroise sea studies, https://doi.org/https://doi.org/10.17882/74004, 2020.

830 Roelvink, J. A. D. and van Banning, G.: Design and development of DELFT3D and application to coastal morphodynamics, Oceanogr. Lit. Rev., 11, 925, 1995.

Rossi, V., Ser-Giacomi, E., López, C., and Hernández-García, E.: Hydrodynamic provinces and oceanic connectivity from a transport network help designing marine reserves, Geophys. Res. Lett., 41, 2883–2891, https://doi.org/10.1002/2014GL059540, 2014.

835 Le Roy, R. and Simon, B.: Réalisation et validation d'un modèle de marée en Manche et dans le Golfe de Gascogne. Application à la réalisation d'un nouveau programme de réduction des sondages bathymétriques, Rapport technique, EPSHOM, 2003.

Saulquin, B. and Gohin, F.: Mean seasonal cycle and evolution of the sea surface temperature from satellite and in situ data in the English Channel for the period 1986–2006, Int. J. Remote Sens., 31, 4069–4093,
840 https://doi.org/10.1080/01431160903199155, 2010.

Takeoka, H.: Fundamental concepts of exchange and transport time scales in a coastal sea, Cont. Shelf Res., 3, 311–326, https://doi.org/10.1016/0278-4343(84)90014-1, 1984.

Thomas, C. J., Lambrechts, J., Wolanski, E., Traag, V. A., Blondel, V. D., Deleersnijder, E., and Hanert, E.: Numerical modelling and graph theory tools to study ecological connectivity in the Great Barrier Reef, Ecol. Modell., 272, 160–174,

845 https://doi.org/10.1016/J.ECOLMODEL.2013.10.002, 2014.

Vanhellemont, Q.: Automated water surface temperature retrieval from Landsat 8/TIRS, Remote Sens. Environ., 237, 111518, https://doi.org/10.1016/j.rse.2019.111518, 2020.

Viero, D. Pietro and Defina, A.: Renewal time scales in tidal basins: Climbing the Tower of Babel, Sustain. Hydraul. Era Glob. Chang., 338–345, 2016a.

850 Viero, D. Pietro and Defina, A.: Water age, exposure time, and local flushing time in semi-enclosed, tidal basins with negligible freshwater inflow, J. Mar. Syst., 156, 16–29, https://doi.org/10.1016/j.jmarsys.2015.11.006, 2016b.

White, L.: Diagnoses of vertical transport in a three-dimensional finite element model of the tidal circulation around an island, Estuar. Coast. Shelf Sci., 74, 655–669, https://doi.org/10.1016/J.ECSS.2006.07.014, 2007.

Yepes-Arbós, X., van den Oord, G., Acosta, M. C., and Carver, G. D.: Evaluation and optimisation of the I/O scalability for

855 the next generation of Earth system models: IFS CY43R3 and XIOS 2.0 integration as a case study, Geosci. Model Dev., 15, 379–394, https://doi.org/10.5194/gmd-15-379-2022, 2022.

Zimmerman, J. T. F.: Mixing and flushing of tidal embayments in the western Dutch Wadden Sea part I: Distribution of salinity and calculation of mixing time scales, https://doi.org/10.1016/0077-7579(76)90013-2, 1 September 1976.

860
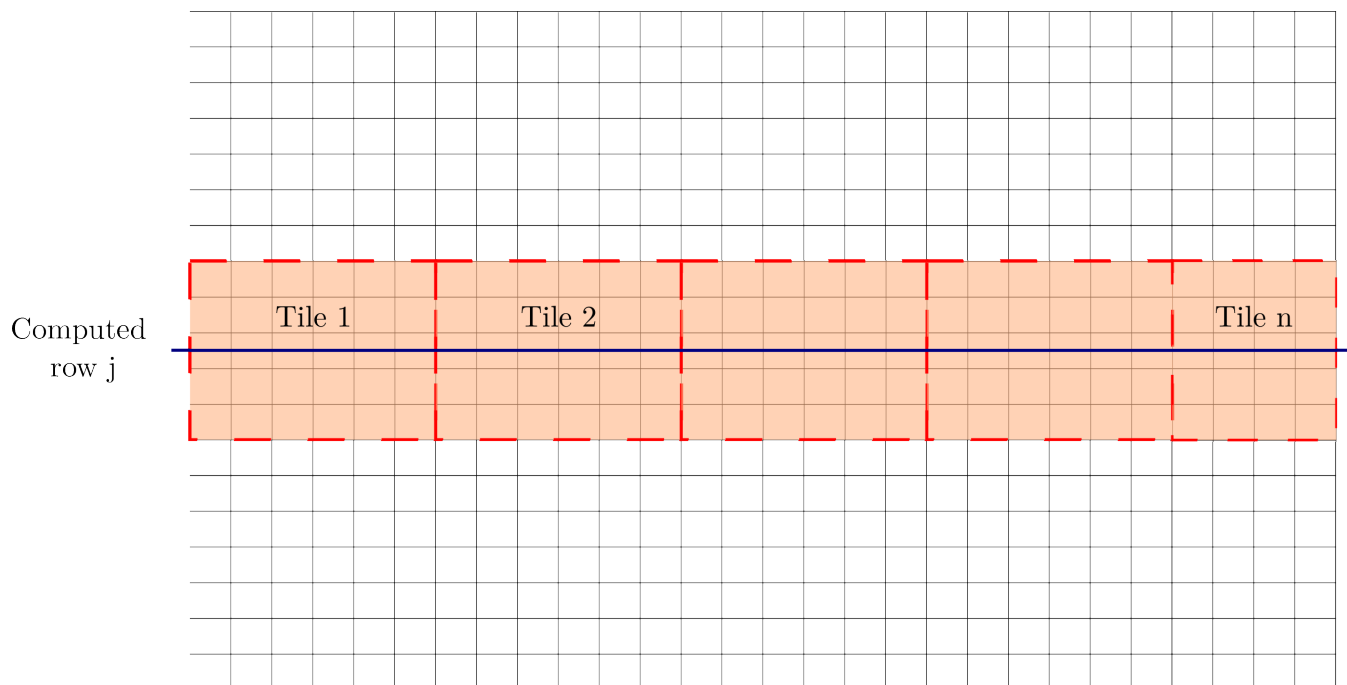
Figure 1: Schematic domain decomposition for solving ADI equation system
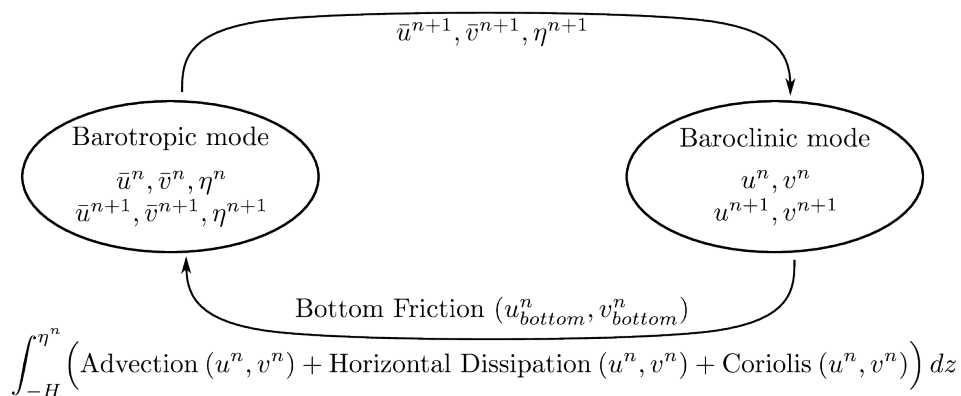

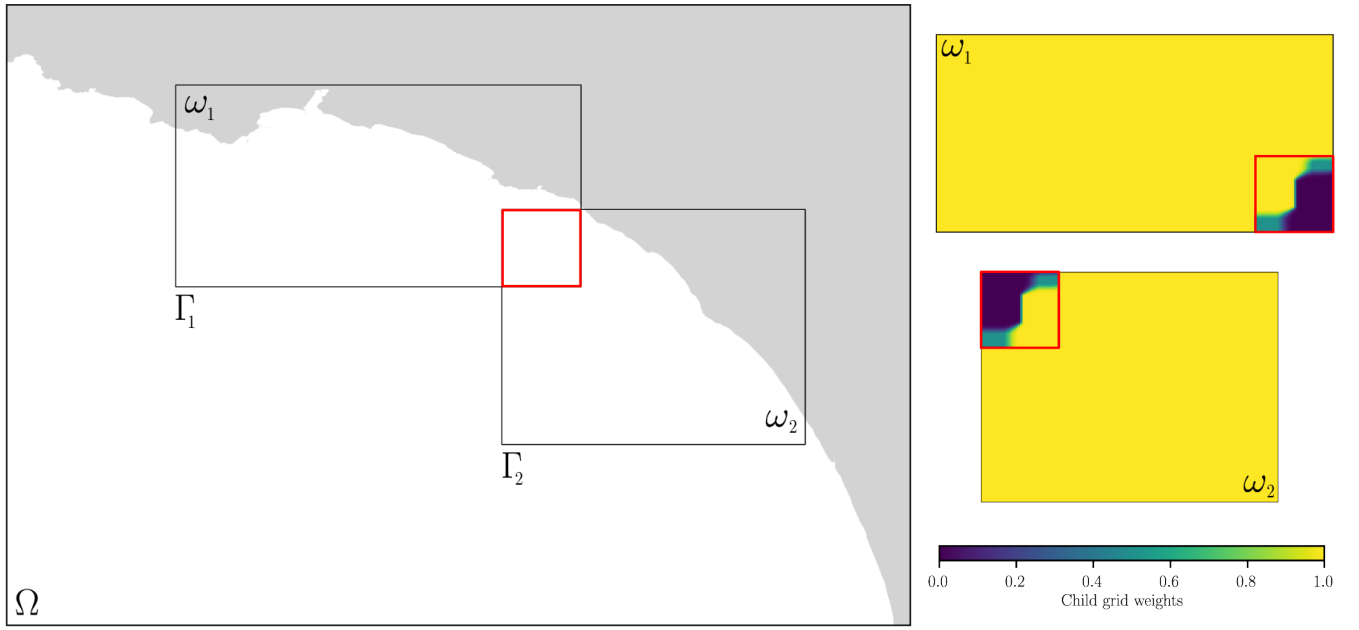**Figure 2: Diagram of the coupling between barotropic and barotropic mode**

Figure 3: On the left, local refinement with two child grids. On the right, the weights used for interaction at same hierarchical level on the overlap area represented with a red rectangle.
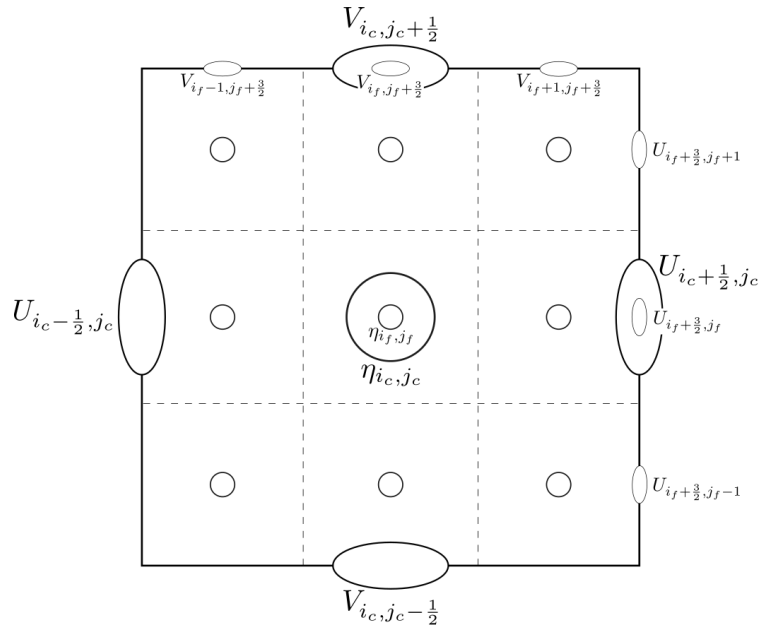
870

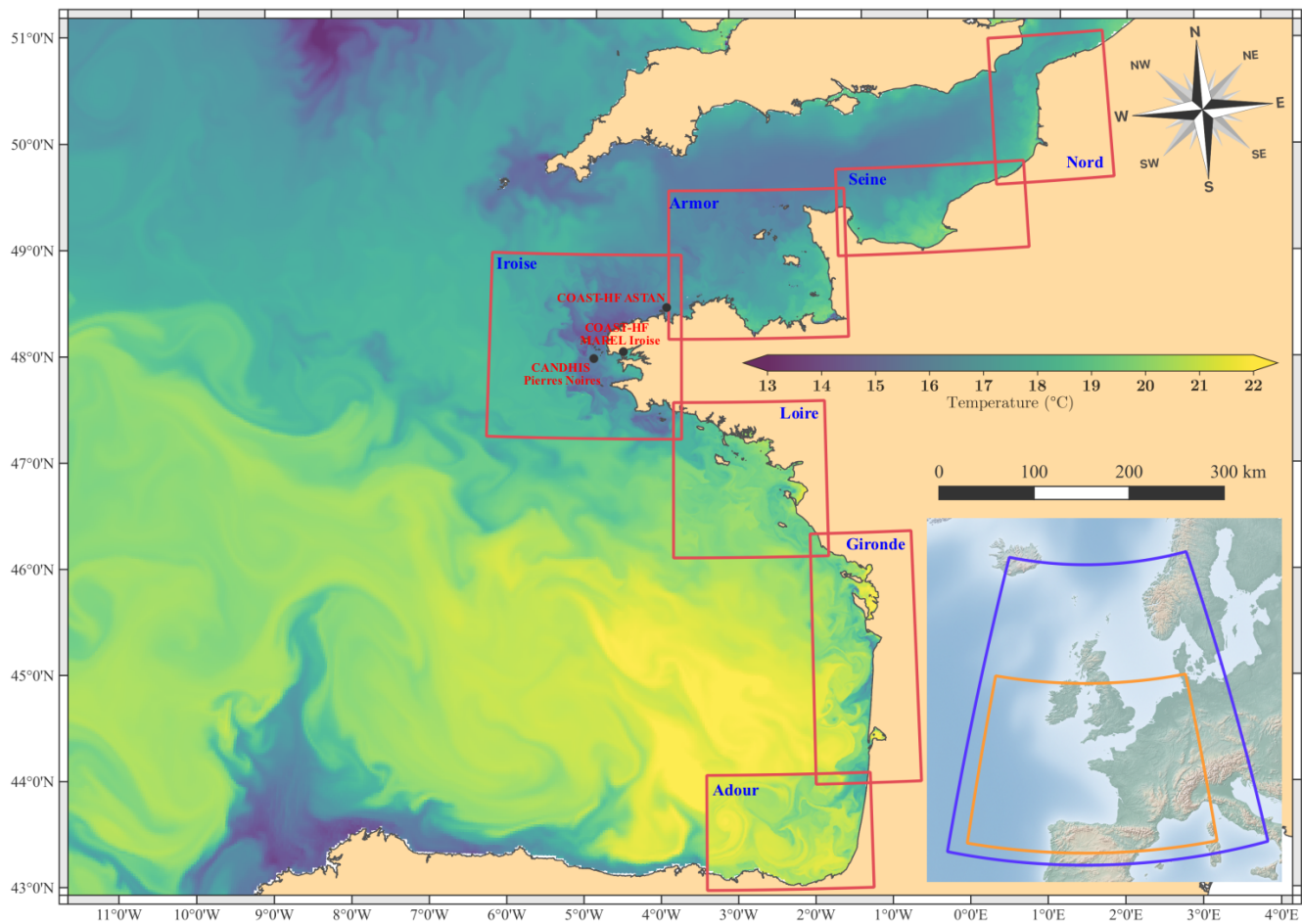**Figure 4: A coarse grid cell divided in nine fine grid cells on a C grid**

31

Figure 5: Bay of Biscay configuration with seven zooms of 500m resolution (red rectangles). The 2.5 km resolution coarser grid (orange rectangle) is included in a larger 2D model at 5 km resolution (blue rectangle). The sea surface temperature is given for the 16th august 2018 with the finest possible resolution. Bathymetric and coastline sources: Ifremer / SHOM / Natural Earth.
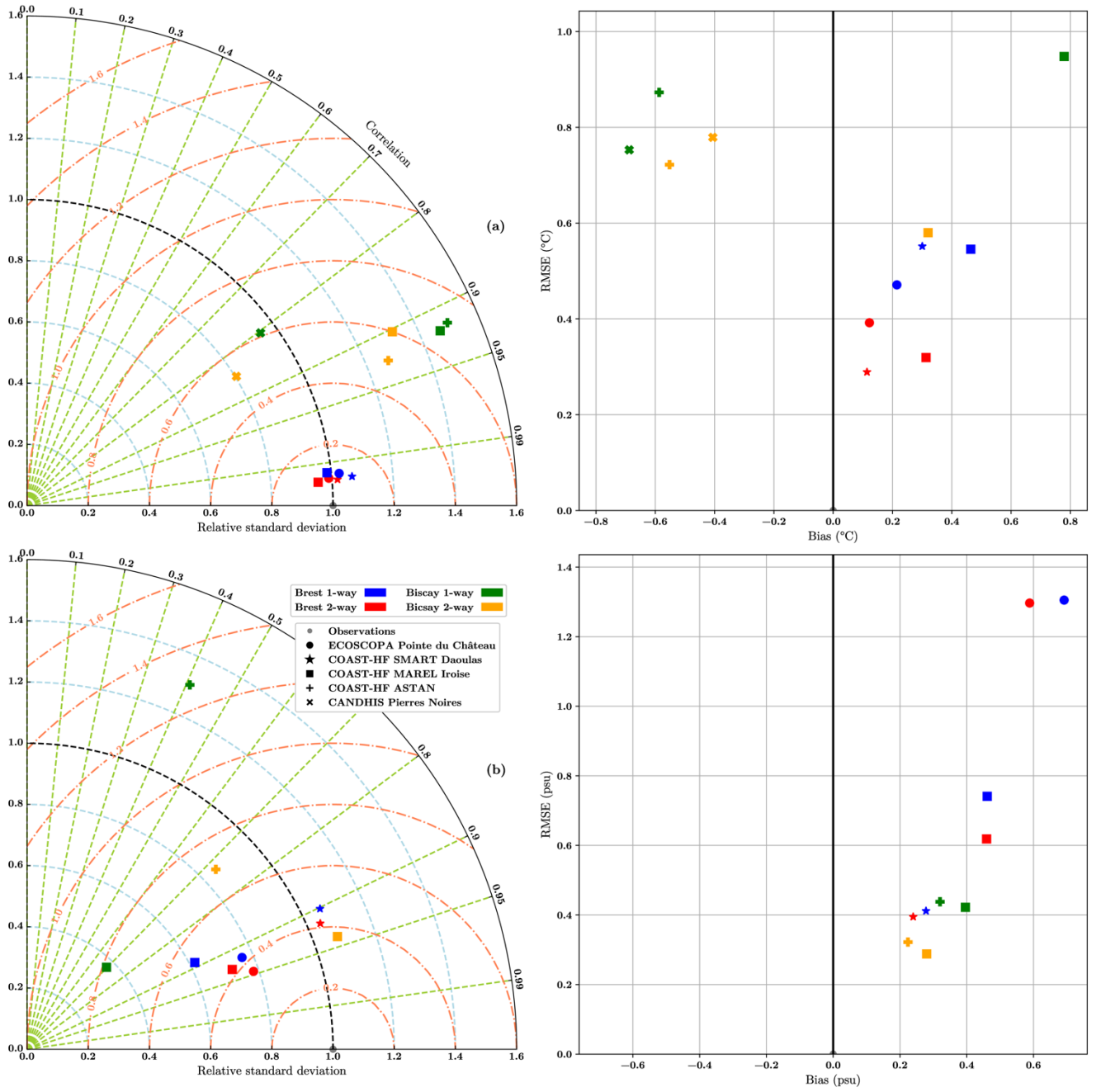
Figure 6: Temperature (a) and Salinity (b) validation for both configurations. The Taylor diagrams are represented with relative standard deviation (blue dashed lines), correlation (green dashed lines) and relative root mean square error (red dashed lines).
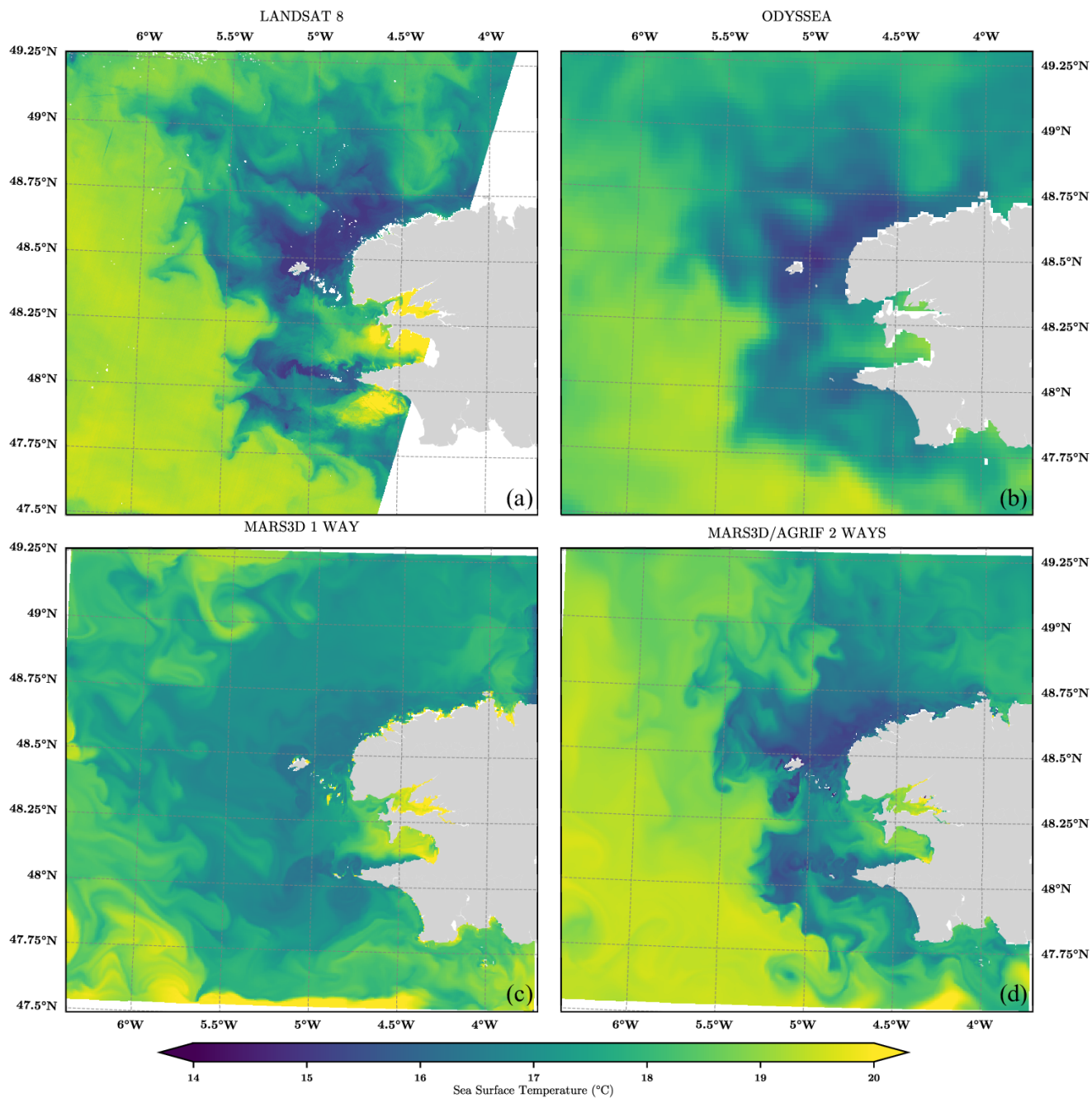
Figure 7: Sea surface temperature over the Iroise sea on August 15th, 2016 for Landsat 8 (a), Odyssea (b), one-way simulation (c) and two-way simulation (d). Coastline source: SHOM.
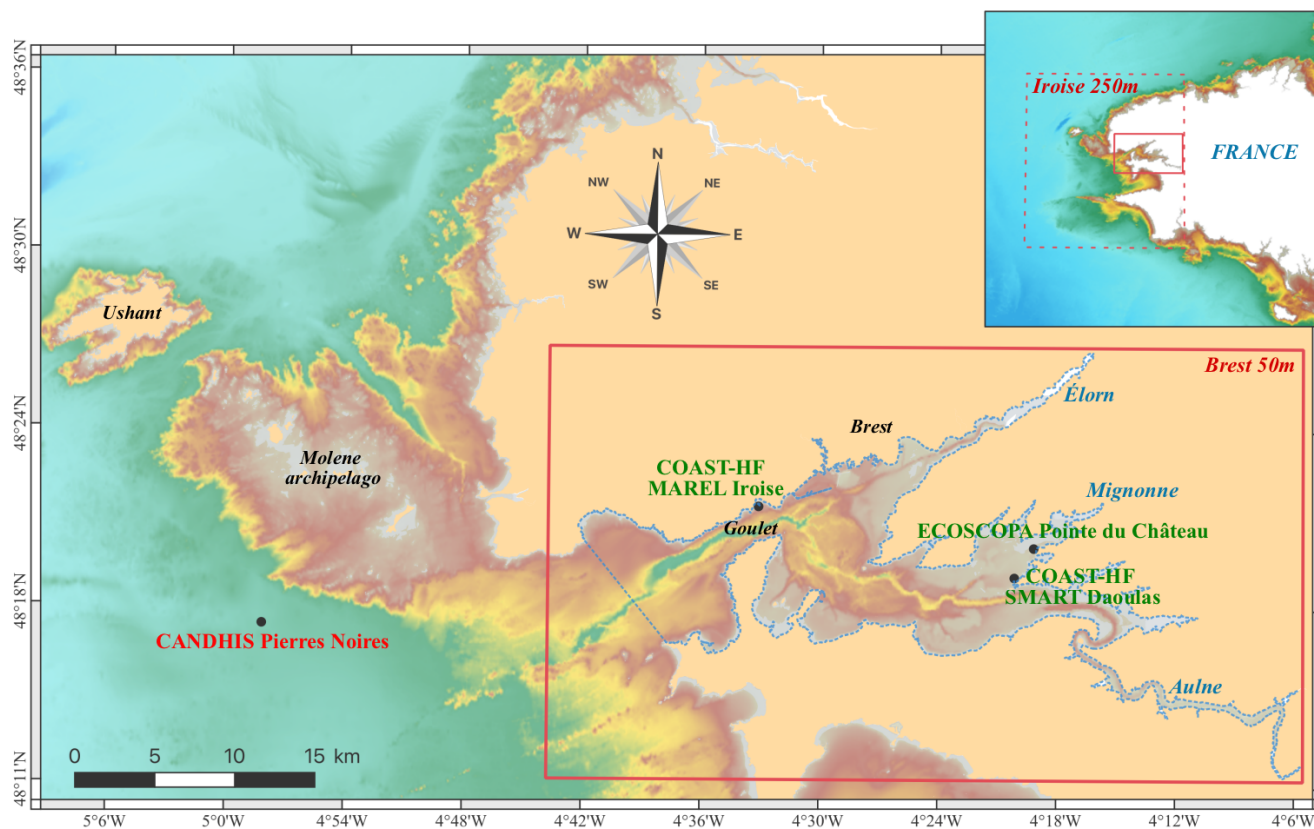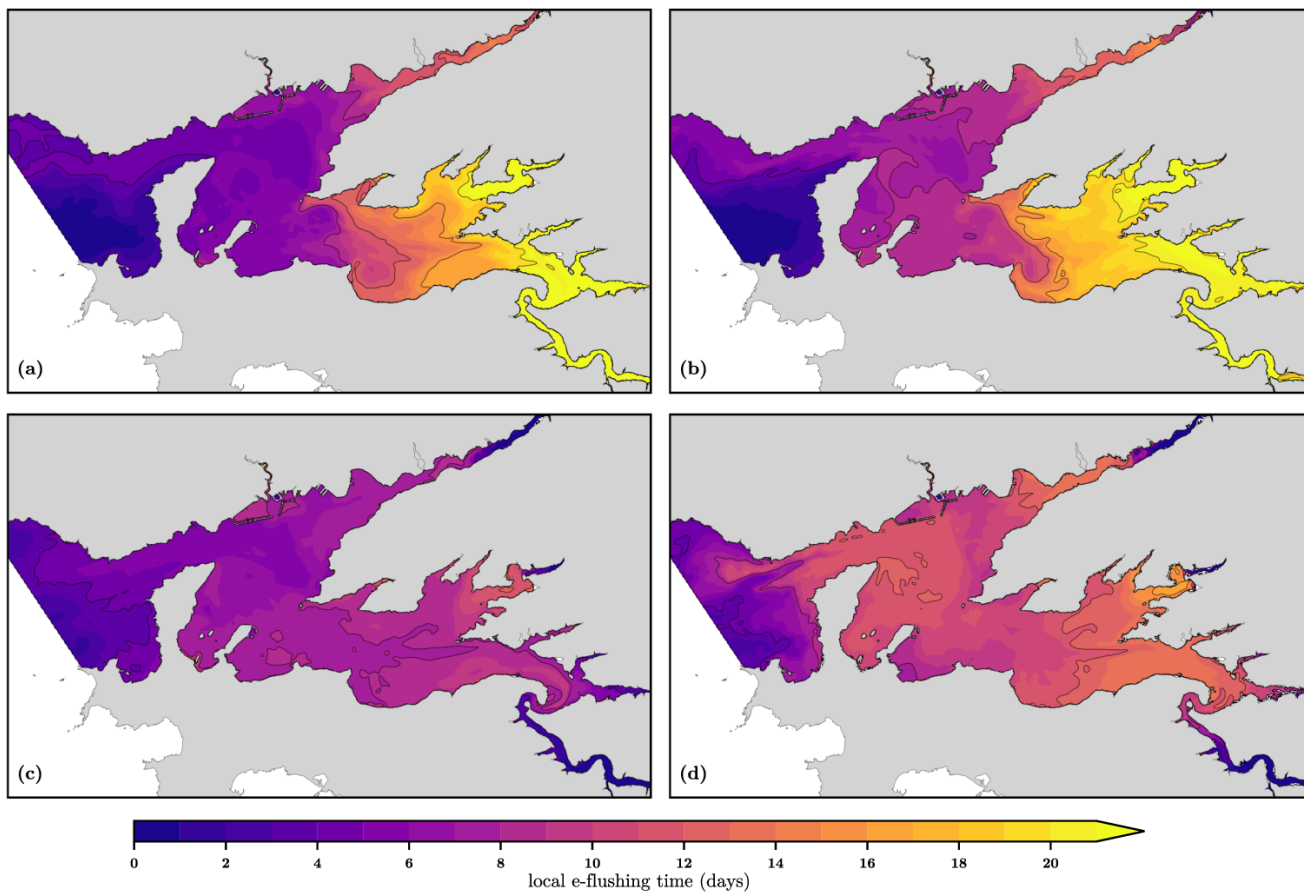
Figure 8: Bay of Brest configuration. The geographic extent of the zoom grid at 50 m resolution is the solid red rectangle. The coarser grid at 250 m resolution is the dashed red rectangle. The dashed blue line represents the control volume used for the estimation of the renewal indicator. Bathymetric and coastline sources: Ifremer / SHOM.

890　Figure 9: Local e-folding flushing time estimated for spring (a) and neap (b) tides in low-flow conditions and for spring (c) and neap (d) for flood conditions. Coastline source: SHOM.
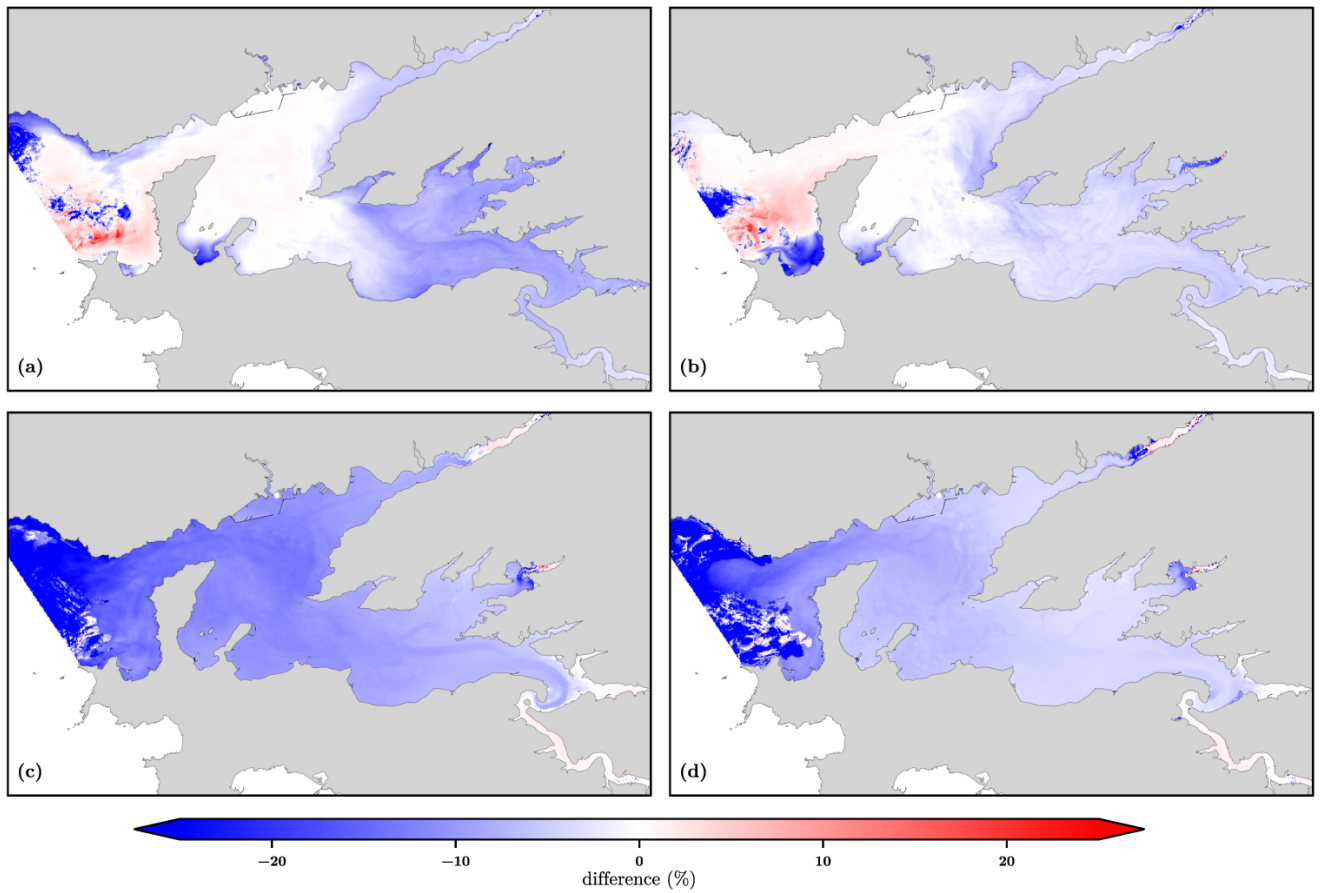
Figure 10: Differences between local e-folding flushing times estimated with one-way configuration over two-way nesting method. They are computed for spring (a) and neap (b) tides in low-flow conditions and for spring (c) and neap (d) for flood conditions. Coastline source: SHOM.